Petroleum Science 23 (2026) 7122–7141

Contents lists available at ScienceDirect

Petroleum Science

journal homepage: www.keaipublishing.com/en/journals/petroleum-science

Original Paper

# Seismic lithofacies classification and fault detection using self-organizing maps and convolutional neural networks in the Penobscot field, Scotian Shelf, Eastern Canada

Tarek Khalifa [a,b], Ahmed Eleslambouly [c,*], Gui-Bin Zhao [c], Amir Ismail [b]

[a] Department of Geology & Geophysics, Texas A&M University, TX, 77843, USA
[b] Geology Department, Faculty of Science, Capital University, Cairo, 11795, Egypt
[c] Department of Earth Sciences, Khalifa University, Abu Dhabi, P.O. Box 127788 UAE

ARTICLE INFO

*Article history:*
Received 25 November 2025
Received in revised form
15 May 2026
Accepted 27 May 2026
Available online 3 June 2026

Edited by Jie Hao

*Keywords:*
SOM (self-organizing map)
Machine learning
Reservoir characterization
Fault detection
Lithofacies prediction
Scotian Basin
HACs (hydrocarbon anomaly clusters)

ABSTRACT

Accurate characterization of lithofacies and fault networks is critical for delineating reservoir architecture, heterogeneity, and compartmentalization in structurally complex hydrocarbon systems. Conventional seismic interpretation methods are often limited by subjectivity and insufficient resolution in complex stratigraphic and structural settings. This study evaluates the effectiveness of an integrated machine learning workflow combining Self-Organizing Maps (SOMs) and Convolutional Neural Networks (CNNs) for seismic lithofacies classification and fault detection in the Penobscot Field on the Scotian Shelf, Eastern Canada. A suite of multi-attribute seismic data derived from 3D post-stack seismic volumes was optimized using principal component analysis and multi-metric dependency assessment prior to SOM training. An 8 × 8 SOM grid was employed to classify seismic facies into 8 lithological classes, calibrated against petrophysical logs and core descriptions from 2 wells. The SOM achieved a high recall (1.00) across key reservoir facies, with precision values ranging from 0.50 to 1.00, reflecting effective discrimination of reservoir and non-reservoir lithologies despite transitional facies mixing. SOM training exhibited stable convergence, with neuron weight shifts stabilizing below 0.1 after approximately 40 training epochs, indicating robust learning of the seismic attribute space. Fault detection was performed using a pre-trained CNN to generate fault probability volumes, which were subsequently refined using Laplacian-of-Gaussian filtering and skeletonization. Integration of CNN-derived structural attributes within the SOM framework enabled near-sample-scale fault delineation (≈8 m vertical resolution) and the isolation of structurally coherent fault planes. The combined SOM-CNN approach enhanced the interpretability of stratigraphic architecture, fault compartmentalization, and hydrocarbon anomaly distribution within Jurassic-Cretaceous reservoir intervals, particularly the Missisauga and Abenaki formations. The results demonstrate that unsupervised learning, when supported by quantitative validation and structural constraints, provides a robust and interpretable framework for high-resolution reservoir characterization in complex offshore settings.
© 2026 The Authors. Publishing services by Elsevier B.V. on behalf of KeAi Communications Co. Ltd. This is an open access article under the CC BY-NC-ND license (http://creativecommons.org/licenses/by-nc-nd/4.0/).

## 1. Introduction

As oil and gas remain the dominant energy source, numerous geoscientific studies have been conducted to explore and develop hydrocarbon reserves to meet the world's growing energy demand (Abdelmaksoud and Ali, 2024; Ali et al., 2024; Ashraf et al., 2020; Eleslambouly et al., 2026a, 2026c; Ikevuje et al., 2024; Song et al., 2024). A significant portion of the remaining hydrocarbon reserves is confined to complex geological settings or deep subsurface environments, making exploration both cost-intensive and high-risk. Consequently, a comprehensive analysis of diverse datasets and methodologies, along with their integration, is essential to characterize reservoir facies and optimize exploration strategies

* Corresponding author.
*E-mail address:* ak.eleslambouly@gmail.com (A. Eleslambouly).
Peer review under the responsibility of China University of Petroleum (Beijing).

https://doi.org/10.1016/j.petsci.2026.05.052
1995-8226/© 2026 The Authors. Publishing services by Elsevier B.V. on behalf of KeAi Communications Co. Ltd. This is an open access article under the CC BY-NC-ND license (http://creativecommons.org/licenses/by-nc-nd/4.0/).

effectively (Eleslambouly et al., 2024a; Gao, 2011; Gilbert et al., 2010; Rotimi et al., 2014).

Traditional lithofacies prediction and fault detection methods rely heavily on seismic interpretation and well-log analysis, which can be subjective, time-consuming, and limited in resolution (Gao, 2011; Hart, 1999). Additionally, seismic attributes provide valuable insights into the subsurface, but extracting meaningful geological patterns from them requires advanced computational techniques and is time-consuming (Chopra and Marfurt, 2005; Subrahmanyam and Rao, 2008). Conventional classification techniques, such as statistical or deterministic algorithms, often require extensive manual input and expert-driven parameterization, which may lead to inconsistencies in the interpretation (Celecia et al., 2021; Khosro Anjom et al., 2024). Moreover, the advancements in seismic data acquisition and processing face a challenge to accurately characterize lithofacies and detect faults due to the inherent noise, resolution limitations, and subjectivity in manual interpretation (Ercoli et al., 2023; Faleide et al., 2021; Michie et al., 2021). Additionally, fault detection using traditional edge detection or curvature-based methods can struggle to delineate subtle or discontinuous faults (Shiney et al., 2025).

In recent years, machine learning has emerged as a powerful tool for enhancing seismic interpretation and processing, enabling geoscientists to identify complex structural and stratigraphical features, improving accuracy and efficiency (An et al., 2023; Eleslambouly et al., 2026b; Lin et al., 2024). Among these techniques, unsupervised learning approaches such as Self-Organizing Maps (SOM) have gained attention for their ability to automatically cluster seismic attributes, revealing hidden patterns that might be overlooked in conventional analysis (Meyer et al., 2022; Zhang et al., 2015; Zhao et al., 2015). Seismic amplitude- and frequency-based attributes have long been used to delineate reservoir facies. Although conventional attributes can distinguish facies to some extent, their reliability decreases when dealing with thin, localized, or heterogeneous reservoir facies, often limiting accurate facies characterization (Eleslambouly et al., 2024c; Oumarou et al., 2021; Owusu et al., 2024; Wu et al., 2012). The SOM technique, first proposed by Kohonen (1982), is an unsupervised neural network that projects high-dimensional data into a low-dimensional, topologically ordered space (Kohonen and Kohonen, 2001; Su and Chang, 2001). SOM has become a valuable tool in geophysical data analysis, particularly for seismic interpretation, where it helps reduce the complexity of multi-attribute datasets while preserving their inherent data structure (Coléou et al., 2003; Roden et al., 2015). SOM provides a robust alternative by clustering high-dimensional seismic attributes into meaningful patterns, enabling the effective identification of lithofacies distributions and fault networks. However, the application of SOM in seismic-driven reservoir characterization is still evolving, and there is a need to evaluate its performance in real-world geological settings.

The Penobscot Field on the Scotian Shelf offshore eastern Canada is a well-documented hydrocarbon prospect with publicly available 3D seismic data and well logs (Fig. 1). The region has a complex geological history, with multiple depositional sequences and structural features, including different tectonic episodes (Brown, 2008; Deptuck and Altheim, 2018; Ellis et al., 1985; Peace et al., 2024). The presence of Jurassic and Cretaceous-aged reservoir units makes it a good candidate for our case study to examine machine learning approaches in seismic interpretation (Campbell et al., 2015b).

The Penobscot field has been previously analyzed for seismic studies and machine learning applications, with numerous investigations contributing to its geological and geophysical understanding. Here, we highlight several key studies in this domain. Khalid et al. (2015) applied amplitude-versus-offset (AVO) analysis to differentiate reservoir from non-reservoir facies and classify fluid types. Similarly, Asim et al. (2016) used spectral decomposition techniques based on Fourier transforms to successfully identify potential hydrocarbon leads in the Wyandot, Dawson Canyon, and Missisauga formations. Further stratigraphic and facies analyses by Qayyum et al. (2015) identified several prospective hydrocarbon intervals in the Penobscot area. Other studies have focused on high-velocity anomalies (Moreno and Galeano, 2019a, 2019b) and applied constrained sparse spike inversion to distinguish lithological variations (Campbell et al., 2015b). Mandal and Srivastava (2018) investigated the structural evolution of the region, emphasizing the creation of accommodation space and the complex deformation history of the area. Their fault-displacement analysis confirmed significant structural complexity with evidence of multiple deformation phases. Similarly, Omeru et al. (2019) analyzed the faults within the Penobscot 3D seismic cube, emphasizing their structural characteristics and propagation patterns. Their study revealed that faulting is primarily controlled by regional tectonic stresses rather than the presence of localized sedimentary features. Additionally, Bhatnagar et al. (2017) examined transfer zone interactions among dominant normal faults within the Penobscot field, while Yagci (2016) used 2D seismic reflection data to enhance the imaging of structural elements, later integrating it with 3D seismic data. Moreover, a comprehensive structural and stratigraphic interpretation of the Penobscot 3D dataset by Peace et al. (2024) identified evidence of both brittle and ductile reverse faulting during the Late Jurassic to Early Cretaceous period, likely driven by compressional forces at the plate boundary. These reverse faults were later reactivated as normal faults during the Late Cretaceous to Paleogene period of salt migration, illustrating an uncommon phenomenon in passive margins. Peace et al. (2024) emphasized that salt migration played a crucial role in reactivating reverse faults and inducing contractional folding in the overlying sequences, further shaping the region's structural evolution.

Advancements in seismic attribute algorithms have created new opportunities to enhance subsurface interpretation through machine learning techniques such as SOM. In particular, integrating multi-attribute analysis enables the discovery of subtle geological features that may be overlooked when relying solely on single-attribute interpretation. This study aims to develop and implement a SOM-based workflow to accelerate field characterization and delineate seismic lithofacies predictions, in addition to mapping the fault network within the Penobscot Field. The approach leverages a combination of 3D seismic data, well logs, and core information to support a more integrated interpretation. Most existing lithofacies and fault-detection approaches rely on supervised deep learning architectures, such as convolutional neural networks (CNNs) and recurrent neural networks (RNNs).

Shi et al. (2024) employed CNNs for lithofacies prediction using data from Southern Sichuan, China. dos Santos et al. (2021) introduced the RNNs for sedimentary facies classification in the Parana Basin, Brazil. These models are data-driven and are typically trained on labeled datasets from specific fields. As a result, these models tend to be case-specific, with limited transferability to other geological settings.

To reduce the dependency on the field-specific dataset, several unsupervised learning methods, such as SOMs, have been widely employed for seismic lithofacies analysis (Ali et al., 2025; Hussain et al., 2022). SOMs are primarily used as topology-preserving exploratory tools rather than as direct lithofacies classifiers. Despite their effectiveness in revealing data structure and facies relationships, such applications of SOMs have largely remained confined to exploratory facies analysis and have not been

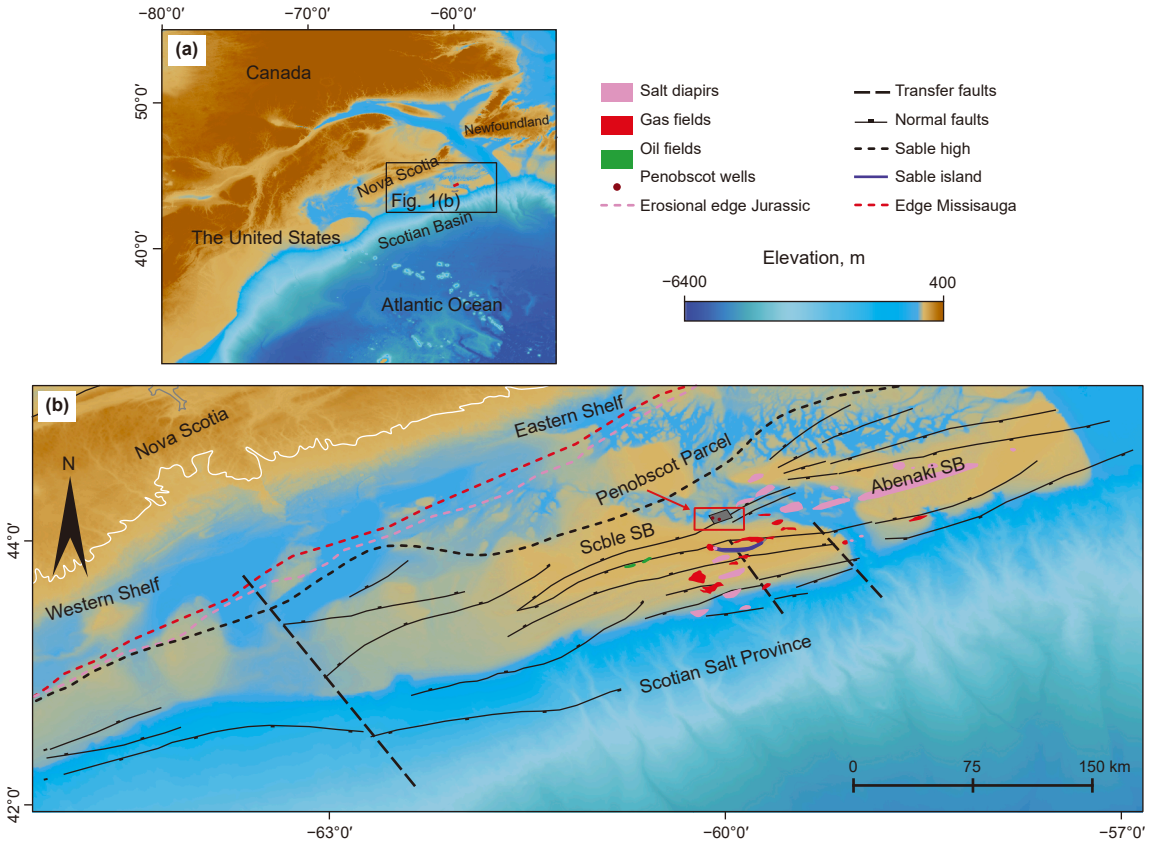



**Fig. 1.** Regional and structural framework of the Scotian Basin and Offshore Nova Scotia. **(a)** Regional elevation map showing the position of the Scotian Basin along the eastern margin of North America, and **(b)** an elevation map of the offshore Nova Scotia area showing major structural elements, the Sable and Abenaki sub-basins (SB). Salt diapirs, transfer faults, and normal fault trends are indicated along with major hydrocarbon fields and offshore wells used in this study. In addition to the Penobscot parcel and seismic boundaries.

systematically extended to integrated lithofacies classification and fault detection frameworks.

This study introduces a hybrid deep-learning and unsupervised framework that integrates Convolutional Neural Networks (CNNs) with Self-Organizing Maps (SOMs) for simultaneous lithofacies classification and fault detection from 3D post-stack seismic data in the Penobscot Field, offshore Nova Scotia. Unlike conventional field-specific supervised models, the CNN component is pretrained on a large, geologically diverse dataset, thereby enhancing generalization and transferability across different depositional and structural settings. The pretrained CNN transforms seismic amplitudes into fault-probability volumes, while the SOM performs topology-preserving clustering to isolate fault-related neurons and lithofacies patterns for enhanced visualization and interpretation.

The proposed framework is applied to a dataset comprising 596,827 seismic samples and is designed to address three primary objectives: (I) evaluate the capability of SOM to resolve subseismic lithofacies heterogeneity and fluid-related seismic responses using optimized multi-attribute inputs; (II) assess the influence of systematic attribute optimization on SOM stability, convergence behavior, and geological interpretability; and (III) integrate CNN-derived fault-probability volumes into the SOM domain to enable joint lithofacies and structural analysis. SOM classifications are calibrated using well logs and petrophysical data, allowing near-sample-resolution mapping of lithological heterogeneity and hydrocarbon-bearing facies.

To achieve these objectives, the workflow emphasizes rigorous seismic attribute selection and optimization by integrating principal component analysis (PCA) and multi-metric inter-attribute dependency analysis. Fault detection is performed using the pretrained CNN and further refined using Laplacian-of-Gaussian filtering and skeletonization to extract geologically meaningful fault planes. These refined fault attributes are subsequently incorporated into the SOM analysis to identify fault-related neurons and improve delineation of fault networks and fault-controlled compartmentalization. Validation against conventional seismic interpretation and petrophysical data confirms the robustness and geological consistency of the proposed SOM–CNN framework in structurally and stratigraphically complex settings characterized by mixed clastic–carbonate systems. Overall, this study demonstrates that the systematic integration of optimized multi-attribute seismic analysis, unsupervised SOM clustering, and CNN-based structural detection provides a reproducible and scalable workflow for high-resolution reservoir characterization and data-driven geological modeling.

## 2. Geological and tectonic setting

The Penobscot field in the Scotian Basin (Fig. 1a) is one of the hydrocarbon fields within the Sable Island perimeter and represents a promising prospect for hydrocarbon exploration in the Atlantic Ocean (Mukhopadhyay et al., 2003; Narayan et al., 2023; Wach and Brown, 2021). The geology of the Penobscot field is highly complex, reflecting the history of tectonic events and sedimentary processes that have shaped the region from the Early Jurassic to the Quaternary. The stratigraphy of the region has been shaped by substantial deformation caused by orogenic events and relative sea-level shifts, resulting in a diverse succession of sand,

shale, and carbonate deposits (Fig. 2a) (Decalf and Heyn, 2023). The field's intricate geological structures result from diverse rock formations and tectonic forces associated with salt migration, which have acted over extensive geological periods (Decalf and Heyn, 2023; Peace et al., 2024; Wu et al., 2023). The field exhibits an E-W trending anticline (Fig. 2c), intersected by three faults aligned parallel to the fold axis. Both wells are located within the field's structural closure (Fig. 2c).

The Scotian Basin evolved through a series of extensional and compressional episodes that began in the Middle Triassic (van Staal et al., 2012; Wade and MacLean, 1990). Initial rifting between North America and Africa generated narrow grabens filled with continental red beds and volcanic flows, culminating in the extensive salt-rich Argo Formation under arid climatic conditions (Asim et al., 2016; Schenk, 1997). By the Early Jurassic, the basin transitioned to shallow-marine settings, leading to the deposition of carbonates along platform margins and hinge zones, most notably in the Abenaki Formation (Eliuk, 1978; Given, 1977). As rifting progressed into the Late Jurassic and Early Cretaceous, the Scotian Basin continued to subside, receiving substantial clastic input that built thick deltaic to shallow-marine successions (Cummings, 2004; Pe-Piper and MacKay, 2006). The Missisauga and Logan Canyon Formations exemplify this period: they are dominated by sandstones interbedded with shales, reflecting high sediment supply from continental sources (Campbell et al., 2015a; Sayers, 2013). These Jurassic–Cretaceous intervals constitute the basin's primary hydrocarbon reservoirs, as they exhibit considerable porosity and permeability in their fluvial-deltaic sandstones (Asim et al., 2016; Eleslambouly et al., 2025; Khalid et al., 2015; Narayan et al., 2023).

Superimposed on this stratigraphic development is a dynamic tectonic framework shaped by both extensional faulting and later compressional forces, as well as pervasive salt movement. The early salt migration events were driven by rapid sediment loading during the Jurassic, resulting in diapirs, pillows, and salt walls that subdivided the basin into multiple structural compartments (Hudec and Jackson, 2006; Shimeld, 2004). These salt-related structures, along with growth faults and inversion features, created numerous structural traps across the Sable Subbasin (Decalf and Heyn, 2023; Peace et al., 2024). In the Penobscot Field specifically, reactivated faults and salt-induced folding have generated four-way dip closures that host accumulations of hydrocarbons (Eleslambouly et al., 2024b; Peace et al., 2024). Reservoirs in the Missisauga and Logan Canyon Formations are charged primarily by organic-rich Jurassic shales in the Verrill Canyon and Eurydice Formations, while thick shales in the Dawson Canyon and Wyandot Formations form the principal regional seals (Deptuck et al., 2014; Kendell and Deptuck, 2012; Narayan et al., 2023). As a result, the Jurassic–Cretaceous interval in the Penobscot Field stands out for its robust hydrocarbon potential, reflecting the long-lived interplay of syn-rift salt deformation, deltaic sedimentation, and subsequent tectonic reorganization that together sculpted the field architecture.

## 3. Dataset

The 3D Penobscot seismic survey within the Scotian Basin spans an area of approximately 86.2 km$^2$ (Fig. 1b). Originally acquired in 1992, the dataset underwent Pre-stack Time Migration (PSTM) processing. It was subsequently reprocessed in 2017 using advanced imaging techniques to enhance subsurface resolution. The seismic data follow the standard (positive) SEG polarity convention, in which reflections corresponding to an increase in acoustic impedance appear as positive peaks (red), while those associated with a decrease in acoustic impedance appear as negative troughs (blue) (Fig. 2b; Ramsey, 2019). The survey records seismic signals with a two-way travel time (TWT) of up to 6 s and a 4 ms sampling interval. The dataset is structured with inline numbers ranging from 1000 to 1600 and crossline numbers from 1000 to 1481, employing a bin size of 12.5 m (inline) × 25 m

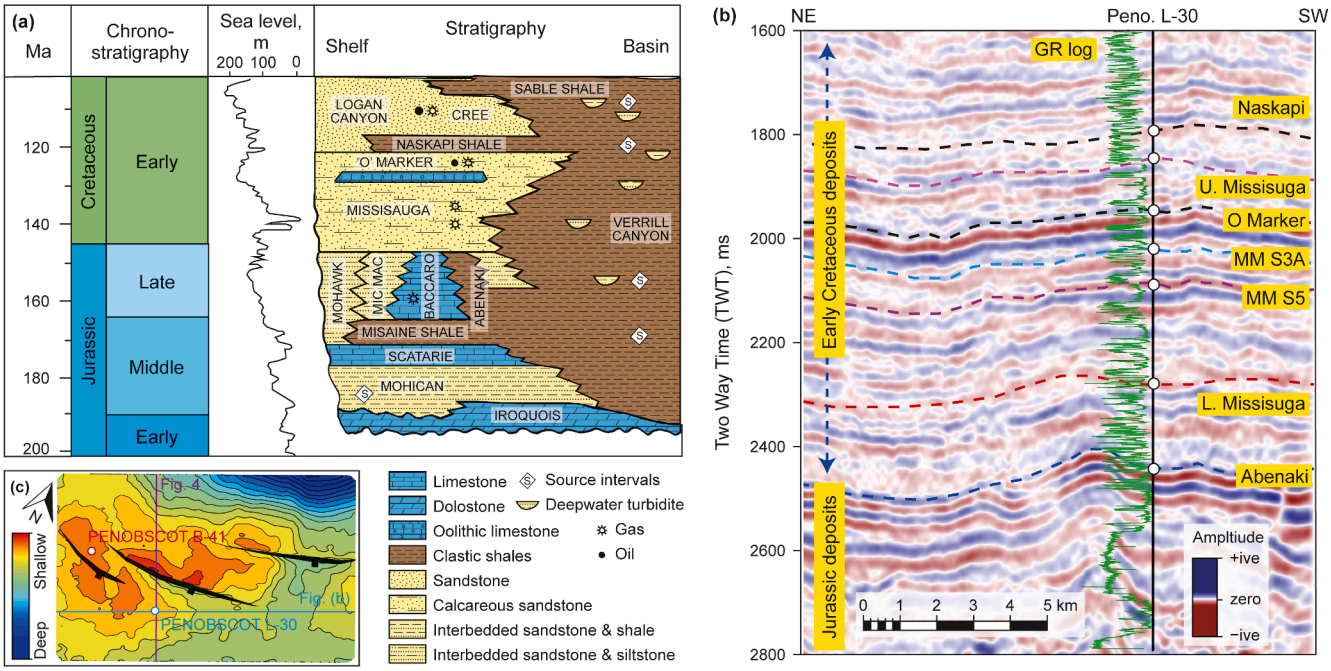



**Fig. 2.** Chronostratigraphy of the Scotian Basin and seismic interpretation of the Penobscot Field for an interval of interest. **(a)** Chronostratigraphic chart of the studied section displaying sea-level variations and key lithostratigraphic units from the Early Jurassic to Early Cretaceous. **(b)** An interpreted inline seismic section along Penobscot L-30 well, showing key horizons, correlated with the gamma-ray (*GR*) log. **(c)** Structural map of the Upper Missisauga Formation illustrating E–W-trending structural highs within the field and potential hydrocarbon traps.

(crossline). The dataset exhibits a high signal-to-noise ratio, with an effective frequency bandwidth of 5–52 Hz for the first 3 s (~5 km depth). However, the signal quality deteriorates significantly beyond this depth due to increasing noise levels.

The 3D Penobscot seismic survey encompasses two drilled wells in the western parts of the seismic cube, namely L-30 and B-41, as illustrated in Fig. 2c. Well L-30, reaching a total depth of 4.2 km, penetrates the Jurassic Abenaki Formation, while Well B-41, drilled to 3.4 km, reaches the base of the Early Cretaceous Missisauga Formation. Publicly available well data for these two wells include a suite of conventional wireline logs, such as caliper, gamma-ray (*GR*), compressional wave velocity, bulk density, spontaneous potential, resistivity, and neutron-porosity logs, as well as checkshot data, formation tops, and core information. These well data are acquired from the Canada-Nova Scotia Offshore Petroleum Board (CNSOPB) and the Geological Survey of Canada (GSC) repositories. Meanwhile, the seismic data are obtained from the open seismic repository of "Terra Nubis" of OpendTect. Moreover, conventional formation evaluation comprising effective porosity ($\varnothing_e$), shale volume ($V_{sh}$), and water saturation logs ($S_w$), lithological classification, and rock-typing logs have also been obtained after the work by Eleslambouly et al. (2025). These logs were utilized to generate an electrofacies log based on petrophysical cutoffs (Eleslambouly et al., 2025). Lithology logs were derived using a cutoff-based (Table 1) classification of key petrophysical parameters across the target interval. This integrated dataset serves as a valuable input for machine learning algorithms for subsurface characterization, reservoir evaluation, and seismic-well integration in the Scotian Basin.

## 4. Methods

In our study, we developed two workflows: one for stratigraphic analysis and one for fault detection. The stratigraphic workflow integrates lithofacies classification with the first-time introduction of Hydrocarbon Anomaly Clusters (HACs), defined as SOM-derived, spatially coherent seismic-anomaly clusters that emerge from the unsupervised organization of multi-attribute seismic responses and are interpreted as indicators of potential hydrocarbon presence. The integration of both approaches provides a refined understanding of the stratigraphic boundaries and structural framework of the seal and reservoir intervals, enabling the precise delineation of key geological features and fluid contacts within the subsurface.

### 4.1. Stratigraphic analysis

The workflow for stratigraphic characterization is illustrated in Fig. 3. A qualitative seismic interpretation was initially performed to identify intervals of interest, guided by the time–depth (TD) relationship derived from checkshot data. This TD calibration is critical for ensuring accurate alignment between seismic data and well data, which forms the foundation for subsequently establishing a direct link between neurons derived from seismic attributes and lithofacies identified in well logs. A subsequent stratigraphic interpretation, based on seismic-to-well ties, identified three key stratigraphic units: the Naskapi Formation, which serves as the upper regional seal; the Missisauga Formation, which hosts the primary hydrocarbon reservoirs; and the Abenaki Formation.

**Table 1**
The petrophysical cutoff ranges used in the SOM-based lithofacies classification. Ranges include gamma-ray *GR*, effective porosity ($\varnothing_e$), water saturation ($S_w$), and shale volume $V_{sh}$ for each identified rock type within the interval of interest.

| Rock Type | *GR* (API) | $\varnothing_e$, % | $S_w$, % | $V_{sh}$, % |
|---|---|---|---|---|
| Sand G1 (Oil sands) | 15 – 53 | 10 – 23 | 11 – 55 | 0 – 34 |
| Sand G2 (Condensate sands) | 11.76 – 69.55 | ≥15 | 11 – 90 | 0 – 50 |
| Sand G3 (Water sands) | 13.4 – 70 | ≥15 | 16 – 100 | 15 – 67 |
| Silty sand | 11.76 – 30 | ≥15 | ≥23 | 0 – 23 |
| Shales | 100 – 138 | 0 – 3 | ≥90 | 55 – 90 |
| Limestone/Shale | 70.03 – 99 | ≥0 | 63 – 100 | 39 – 73 |
| Siltstone | 70.01 – 99 | ≥5 | 12 – 30 | 36 – 69 |
| Claystone | 100.16 – 122 | ≥0 | ≥90 | 68 – 99 |

Furthermore, the post-stack seismic volume is utilized to generate both instantaneous and spectral decomposition (SD) attributes. As emphasized by Zhao et al. (2015), SD attributes play a pivotal role in this study, offering enhanced interpretive capabilities by transforming broadband seismic signals into discrete-frequency components. This frequency-targeted analysis improves vertical resolution and facilitates the delineation of subtle stratigraphic features, including incised channels, thinly bedded sand bodies, and heterogeneities that are often obscured in conventional broadband data (Gorain and Shalivahan, 2018). Instantaneous seismic attributes, derived through complex trace analysis, included reflection strength (envelope), instantaneous phase, and instantaneous frequency (Barnes, 2016). A total of 60 highly sensitive attributes to lithologic variations, reservoir property changes, and thickness variations were derived from the seismic dataset (Chopra and Marfurt, 2006; Oumarou et al., 2021). These attributes consist of 49 spectral decomposition attributes and 11 instantaneous attributes (listed in Table S1). These complex trace attributes enable interpreters to visualize seismic data characteristics in ways previously not possible, laying the foundation for a wide range of derivative seismic attributes.

However, the initial set of 60 attributes introduced redundancy due to inter-attribute correlations, thereby increasing computational complexity and impeding efficient SOM training. To mitigate redundancy while retaining geologically significant information, principal component analysis (PCA) was applied as a preprocessing step (Babikir et al., 2022). To promote faster convergence and suppress noise associated with minor variance components, a relatively low cumulative variance threshold of ≥50% was selected. This threshold reduced the original 60 attributes to 24 attributes (Table S2), corresponding to an approximate 60% reduction in input dimensionality. This dimensionality reduction reduced the computational burden of distance calculations between input vectors and SOM neuron weight vectors during training. Consequently, SOM training exhibited faster and more stable convergence, with neuron weight updates stabilizing earlier in the training process. The 24 retained attributes included high-impact spectral decomposition attributes, such as spectral magnitude, voice, envelope, and maximum entropy, as well as key instantaneous attributes, such as envelope, instantaneous frequency, relative acoustic impedance, and sweetness.

To ensure interpretive relevance and minimize noise, the analysis was constrained to a targeted seismic window. From the eigenvalue spectrum, 24 attributes were identified as principal contributors (Table S2), selected based on a threshold of ≥50% cumulative variance to ensure optimal retention of independent geophysical information (Roden et al., 2015; Xu et al., 2019). These included high-impact spectral decomposition attributes, such as spectral magnitude, voice, envelope, and maximum entropy, as well as key instantaneous attributes, such as envelope, instantaneous frequency, relative acoustic impedance, and sweetness. Meanwhile, to assess statistical dependency, redundancy, and information content among the 24 seismic attributes, we introduce a comprehensive correlation analysis with three metrics (Pearson

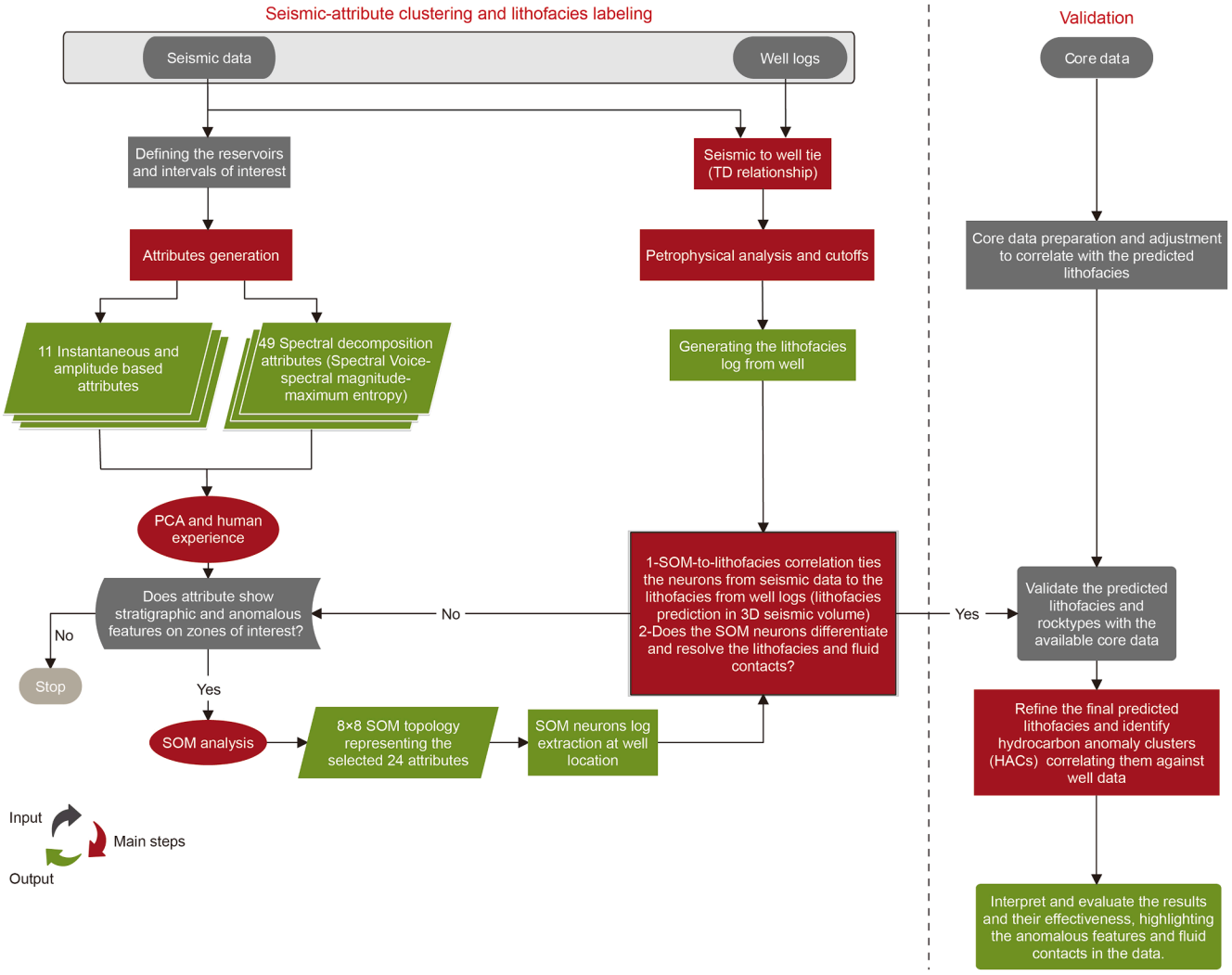



**Fig. 3.** A flow chart describing the workflow used for lithofacies prediction and hydrocarbon anomaly detection utilizing a machine learning-based seismic attribute analysis. The process integrates full-stack 3D seismic data, well logs, and core data to classify and predict the various lithofacies in the field under study.

correlation, Spearman rank correlation, and Mutual Information (MI)), which was performed to follow an approach and classification described by Kim et al. (2019) and further discussed in Table S3. Furthermore, to improve interpretability, systematically reducing the initial set of 60 attributes to an optimized subset of 24 attributes yielded measurable computational efficiency gains.

Pearson's correlation coefficient ($r$) represents linear dependencies. High values ($r > 0.9$) indicated redundancy and potential overlap in spectral or amplitude-based information (Jo et al., 2019; Smith, 2015). The Pearson correlation matrix (Fig. S1) revealed significant linear redundancy between spectral attributes such as CWT Magnitude and Voice components at identical frequencies ($r \approx 0.98$–$0.99$), as well as between Amplitude and Envelope ($r \approx 0.80$), supporting the exclusion of one attribute in each pair to improve model interpretability. Spearman's rank correlation ($\rho$) could identify nonlinear monotonic trends, such as those arising from amplitude envelope or phase effects. In contrast, Spearman's rank correlation (Fig. S2) detected strong nonlinear monotonic dependencies, for example, $\rho \approx 0.84$ between Amplitude and Envelope despite a lower linear correlation ($r < 0.5$), highlighting the potential contribution of phase and tuning effects not captured by Pearson's metric.

MI is able to capture more complex or nonmonotonic dependencies (Gao et al., 2015; Hjelm et al., 2018). MI analysis (Fig. S3), computed via histogram-based entropy estimation, revealed significant nonmonotonic dependencies (MI > 7) between SD CWT Magnitude and Voice components at adjacent frequencies (e.g., 35 Hz). These relationships suggest that while such attributes exhibit weak linear correlation, they retain substantial nonlinear geological information.

Hence, attributes with high MI but low Pearson and Spearman correlations were prioritized for their potential to encode subtle lithological variations or nonlinear tuning effects often missed by linear metrics (Table S4). The lithofacies classification consists of two principal stages: attribute clustering by SOM and lithofacies labeling. Table 2 shows the SOM-based seismic-attribute clustering process. At first, seismic samples around two wells are collected, and each sample is transferred to a 24-dimensional vector of selected attributes, which are then input into the SOM.

The SOM topology was evaluated starting with a smaller 6×6 configuration and progressively increasing to 8×8 and 12×12,

**Table 2**
The SOM seismic-attribute clustering process.

| Steps | Processes and results |
|---|---|
| 1 | Normalization of the input data and initialization of the network parameters |
| 2 | Find the weight vector with the smallest distance from the input vector and define the winning neuron. |
| 3 | Adjust the weights in the neighborhood of the winning neuron to bring it closer to the input vector. |
| 4 | Shrink the neighborhood radius, reduce the learning rate, repeat the training iterations, and output the attribute clustering results. |

using normalized efficiency metrics and training-error behavior, including convergence efficiency, compactness efficiency, utilization efficiency, stability efficiency, information efficiency, training economy, quantization error, and topographic error (Figs. S4–S5, Table 3). For the Penobscot dataset, the 8×8 SOM model was trained using 24 selected seismic attributes and classified 596,827 samples. This configuration achieved full utilization and stability efficiencies of 1.0, confirming that all neurons were active and no samples remained unclassified (Fig. S4). The convergence efficiency of 0.523 indicates effective reduction of initial feature-space disorder, while the high information efficiency of 0.93 demonstrates that the selected attributes preserve strong seismic-structural information.

The quantization error curves decrease progressively with training epoch for all tested grid sizes, confirming stable SOM learning (Fig. S5a). However, the 8×8 model provides an effective balance between representation accuracy and model complexity. Smaller grids, such as 4×4 and 6×6, produce coarser but more compact clustering. In contrast, larger grids, such as 10×10, provide increased resolution but only limited additional reduction in quantization error and a greater risk of over-segmentation. The topographic error curves also support the 8×8 selection. The 8×8 model shows a strong reduction in topographic error and reaches one of the lowest final TE values, indicating good preservation of neighborhood relationships in the seismic attribute space (Fig. S5b). The efficiency metrics, quantization-error behavior, and topographic-error behavior indicate that the 8×8 configuration provides the most balanced trade-off between stability, resolution, training economy, topology preservation, and geological interpretability (Table 3). Therefore, the 8×8 SOM topology was selected as the most suitable configuration for the Nova seismic attribute dataset.

The SOM was trained using an online (sequential) learning scheme, in which neuron weight vectors are updated incrementally after each input sample. This training mode is well-suited for large, high-dimensional seismic datasets, as it preserves topological relationships while enabling stable convergence. A hexagonal neighborhood topology was adopted to ensure smooth lateral transitions between neurons and to minimize directional bias in the mapped lithofacies patterns. The neighborhood influence followed a Gaussian neighborhood function, with an initial neighborhood radius of 7 neurons to promote global ordering during early training stages, followed by exponential decay controlled by a neighborhood decay factor ($\tau_1 = 10$) to refine local lithofacies distinctions progressively. Neuron weights were initialized using a random initialization strategy, ensuring unbiased sampling of the seismic attribute space and avoiding the introduction of a priori geological assumptions. The initial learning rate ($\eta_0$) was set to 0.3 and decayed exponentially with a decay factor ($\tau_2 = 10$), providing stable convergence while preventing oscillatory behavior during late-stage training. The SOM was trained for 100 epochs without early stopping, and convergence was confirmed through stabilization of neuron weight updates, zero dead neurons, and consistent neuron–lithofacies associations.

SOM performed 100 training iterations and output the seismic-attribute clustering results. Fig. S6 illustrates the convergence behavior of the SOM training applied to the seismic data. The rapid decay in neuron shifts during the early training phase suggests a quick separation of spectrally distinct facies. However, several mid-training fluctuations indicate that many lithofacies initially overlapped spectrally, particularly where shales, clastic shale, and carbonates exhibit similar attribute responses (van der Meer, 1996; Wang and Carr, 2012). The final neuron shift value below 0.1 after ~40 epochs confirms that the SOM has reached a stable topological configuration with no dead neurons. This convergence behavior implies that the SOM successfully learned (Jamil et al., 2023; Miyoshi et al., 2002) nuanced seismic signatures and was able to distinguish lithologies such as silty sands, siltstones, and shale/carbonate transitions, despite their subtle textural differences, which are found to be consistent with observations by Kim et al. (2019).

Following SOM-based clustering of seismic attributes, each neuron was assigned to a lithofacies label based on the distribution of lithofacies percentages within that neuron (Fig. 4). The lithofacies composition of each neuron was determined by evaluating the statistical similarity between the seismic-attribute distribution represented by the neuron and petrophysical parameters derived from well-log data. The similarity was quantified by calculating the overlap between their respective probability density functions (PDFs). Petrophysical parameters collected from the two wells, including $GR$, $\varnothing_e$, $S_w$, and $V_{sh}$ overlap across several lithologies, as shown in Table 1, and thus lithofacies cannot be differentiated by single-parameter thresholds. In contrast, the probabilistic framework enables discrimination among lithologies with similar petrophysical ranges by accounting for their joint statistical distributions (Fig. S7). For each neuron, the lithofacies with the highest percentage was designated as the neuron's class, summarized in Table S5. Notably, the emergent HACs reflect coherent lithological patterns across spatially adjacent neurons. For instance, neurons 49 and 50 were dominantly associated with the Sand G1 facies, while neurons 44, 35, and 33 corresponded closely with the mixed Limestone/Shale class.

To validate the neuron-facies associations, the SOM-derived classification was cross-compared with detailed core descriptions. Since the SOM operates at an effective vertical resolution of ~8 m (corresponding to a 4 ms sampling interval), while core data were acquired at sub-meter resolution (<0.5 m), direct

**Table 3**
Performance comparison of SOM grid sizes after 100 training epochs based on quantization error (QE) and topographic error (TE).

| Grid size | Training epochs | Quantization error (QE) | Topographic error (TE) | Comments |
|---|---|---|---|---|
| 4×4 | 100 | 0.1984 | 0.1631 | Coarsest topology; moderate QE but highest TE, indicating weaker topology preservation. |
| 6×6 | 100 | **0.1926** | 0.1085 | Lowest QE, indicating compact representation, but less topologically stable than 8×8. |
| 8×8 | 100 | 0.1974 | **0.0908** | Best TE and balanced QE; strongest topology preservation and best interpretability. |
| 10×10 | 100 | 0.2124 | 0.1276 | Highest QE and increased TE, suggesting over-fragmentation and reduced efficiency. |

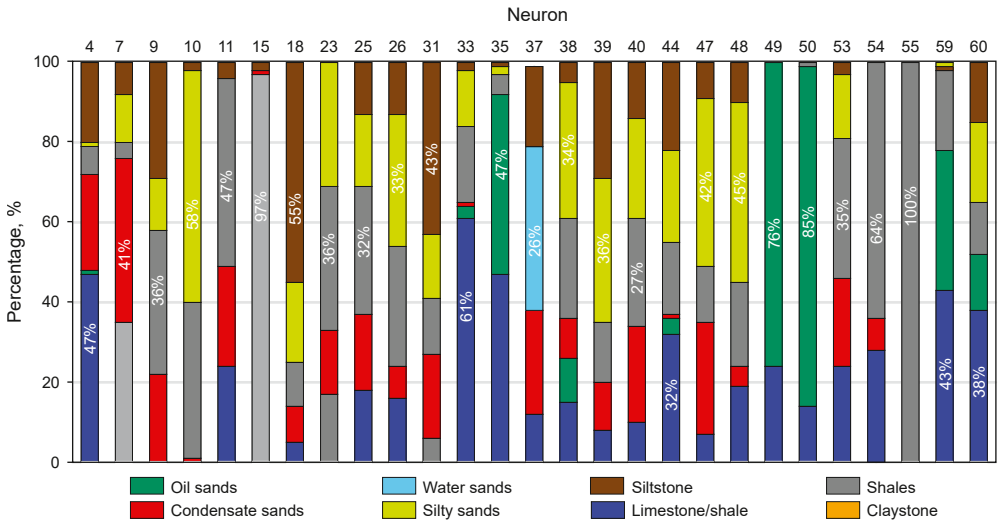



**Fig. 4.** Stacked bar chart showing the lithofacies contribution for each neuron of interest used in the SOM classification. Each bar represents a neuron subdivided by the proportional contribution of different lithofacies classes, expressed as percentages.

comparison required vertical alignment. Core-derived lithofacies were thus upscaled and resampled to match the SOM resolution, enabling a meaningful, resolution-consistent cross-validation. The SOM-classified seismic volume reveals coherent, geologically consistent lithofacies patterns that correlate with well log interpretations from L-30 and B-41. The performance of the SOM-based lithofacies classification within discrete cored intervals between 2500 m and 2700 m in the reservoir, using core-calibrated data from well B-41, is summarized in Fig. S11. We calculated the precision, recall, and F1-score for three key lithofacies classes: limestone/shale, oil sands (Sand G1), and condensate sands (Sand G2). The classification model exhibits robust recall across all facies, achieving a perfect score of 1.00, indicating that nearly all true samples in each facies were correctly identified by the SOM. Precision scores, however, vary across classes, with Sand G1 (oil sands) achieving the highest precision (1.00), followed by Sand G2 (0.67) and limestone/shale (0.50) (Fig. S11a). The lower precision for the latter two suggests some degree of class mixing, likely due to overlapping feature distributions and transitional lithologies. The confusion matrix normalized by row (true classes), highlights the prediction fidelity across the lithofacies. All Sand G1 samples were correctly classified (100%), while 83% of Sand G2 (condensate sands) samples were correctly predicted, with 17% misclassified as limestone/shale. The model shows good separation between sands and non-reservoir facies, especially between the G1 and G2 classes, indicating effective discrimination between oil- and condensate-prone intervals.

### 4.2. Structural interpretation

The workflow for structural interpretation integrates both pre-conditioning and post-processing phases, as shown in Fig. 5. We test the proposed workflow at Inline 1364 as shown in Fig. 6. Initially, the seismic amplitude data (Fig. 6a) undergo a structured pre-conditioning process using 3D-structurally oriented filtering (SOF3D), which sharpens fault discontinuities and suppresses noise artifacts in the seismic volume (Fehmers and Höcker, 2003). Fig. S12 illustrates the seismic amplitude section from the study volume before and after pre-processing and filtering alongside the rejected noise. This particularly enhances the subtle fault signatures in complex or noisy datasets, preserves reflector continuity, and suppresses incoherent noise.

Following data conditioning, fault detection was performed using U-Net Convolutional Neural Networks (CNNs) to identify and delineate faults directly from 3D seismic data (Gao et al., 2022; Qi et al., 2017). A pre-trained CNN, originally developed and trained using SEAM synthetic data that provides controlled fault geometry and the Great South Basin field, following the work of Zhao and Mukhopadhyay (2018), was employed to generate fault probability volumes (Fig. 6b). The CNN is free of interpreter bias and thus significantly reduces the uncertainties associated with traditional manual fault picking (Waldeland et al., 2018).

The CNN-based fault detection model is applied exclusively in inference mode in this study. Consequently, training-related hyperparameters such as learning rate, optimization scheme, batch size, and weight initialization are not user-defined and are not modified within the present workflow. The network was originally trained on a balanced subset of the SEAM synthetic dataset, comprising approximately 20% fault and 20% non-fault samples, totaling ~350,000 training samples, ensuring robust generalization to structurally complex seismic settings. The adopted architecture follows a patch-based CNN architecture for binary fault/non-fault classification, using 2D seismic patches of size 32 × 32 pixels as input. The network consists of a single convolutional layer with a 9 × 9 kernel and 16 feature maps, followed by 2 × 2 max pooling, a fully connected layer with 1024 neurons, and a SoftMax output layer optimized using a cross-entropy loss function.

Following CNN-based fault classification, post-processing was applied to improve the structural accuracy and geological coherence of the derived fault probability volumes. This stage employed fault enhancement and skeletonization algorithms to convert the probabilistic outputs into geologically consistent fault frameworks with improved continuity and edge definition. A directional 3D Laplacian of Gaussian ($LoG_{3D}$) filter is applied to enhance fault features along their primary orientation (Laudon et al., 2021; Mora et al., 2022b). The 3D directional LoG filter, composed of a Gaussian operator for smoothing and a Laplacian operator for sharpening

$$LoG_{3D}(x;\sigma) = \nabla^2(G(x;\sigma)) \quad \text{Eq. 1}$$

where $G(x;\sigma)$ is a 3D Gaussian smoothing kernel with scale $\sigma$, and $\nabla^2$ denotes the Laplacian operator. As a result, this process enhances fault discontinuities parallel to their primary structural

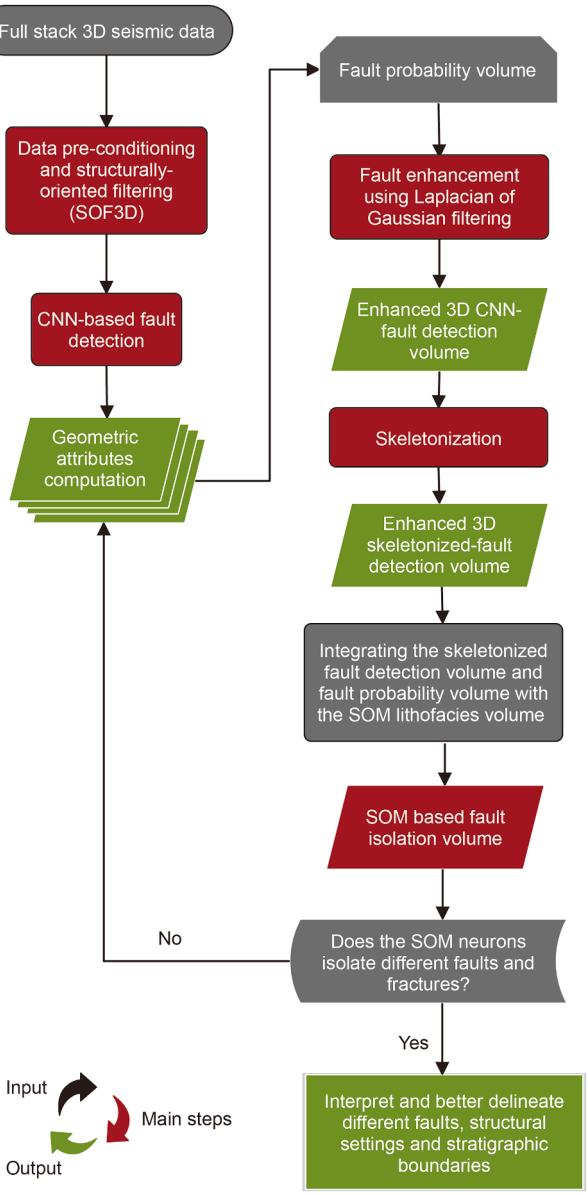



**Fig. 5.** A flowchart shows a deep learning-based fault detection workflow that integrates 3D seismic data with convolutional neural networks (CNNs) for fault identification, and self-organizing maps (SOMs) for fault isolation and classification.

trend, while simultaneously attenuating noise and non-planar features (Fig. 6c). Subsequently, a skeletonization algorithm is employed to extract the central axes of these enhanced fault features (Zhu et al., 2022). Skeletonization is applied in the direction perpendicular to the fault planes, effectively reducing volumetric representations of faults to geologically relevant fault skeletons (Lister, 2004). The outcome of this post-processing workflow consists of three high-resolution skeletonized fault-attribute volumes: fault probability, fault dip magnitude, and fault dip azimuth. These outputs provide a more robust representation of subsurface fault geometry (Fig. 6d). This process helps isolate coherent fault planes and suppresses false positives, particularly those associated with non-planar reflector noise or artifacts.

In the final step, the CNN-derived fault probability volume and the skeletonized fault volume are integrated with the SOM-classified stratigraphic volume, which are introduced as input attributes for the SOM analysis algorithm. This integration of the three input volumes listed in Table 4 allows the extraction of the maximum benefits of a combined structural and stratigraphic interpretation, facilitating a more comprehensive understanding of their interplay at higher spatial resolution. The fault neurons of the SOM spatially correlate with high fault probability (Fig. 6e) and the presence of a skeleton, which enables the isolation of discrete fault planes (Fig. 6f). The SOM analysis algorithm is used to provide unbiased interpretation representative of the detected faults as discrete, isolated fault features, referred to as fault neurons, which are directly linked to key stratigraphic elements within the study interval.

For SOM-based fault-neuron isolation, three input volumes were used as attributes: the CNN fault-probability volume, the skeletonized fault-probability volume, and the SOM stratigraphic-classification volume. The first two inputs are structural fault-sensitive attributes, whereas the third input provides stratigraphic context. The CNN fault-probability volume was generated during the CNN fault-detection pre-processing workflow and represents the main structural discontinuity attribute. The skeletonized fault-probability volume was derived from post-processing of the CNN probability volume and emphasizes the centerline geometry and continuity of the detected faults. In contrast, the SOM stratigraphic classification volume was derived from an independent stratigraphic SOM analysis and included to help distinguish fault-related discontinuities from stratigraphic or facies-related seismic patterns.

Before training the fault-focused SOM, the three input volumes were normalized to a common numerical scale to prevent any single attribute from dominating the clustering solely because of its original amplitude or probability range. No manual weighting was imposed between structural and stratigraphic attributes before SOM training. Instead, the SOM was allowed to cluster the normalized multidimensional feature vectors in a data-driven manner. Neuron-level contribution analysis was then used to evaluate which attributes controlled each neuron. In the fault-sensitive neurons, the CNN fault-probability volume contributed approximately 70.5%-72.8%, the skeletonized fault-probability volume contributed approximately 19%-20%, and the SOM stratigraphic-classification volume contributed approximately 8-10%. This confirms that structural attributes primarily control the isolated fault neurons, while the stratigraphic SOM-classification volume acts as a secondary contextual attribute for separating structural faults from stratigraphic variability.

Hence, the CNN model effectively captured both major and subtle discontinuities, while subsequent SOM clustering further isolated structurally coherent fault patterns. This integration reduced interpreter bias and improved the assessment of compartmentalization and fault-sealing behavior across depth intervals. This integrated model facilitates a deeper understanding of fault-induced reservoir segmentation, potential fluid-migration pathways, and sealing integrity. These observations validate the effectiveness of the CNN-derived fault probability model and its skeletonization in isolating discrete fault structures using SOM classification, which aligns with geologic reality.

## 5. Results and interpretation

### 5.1. SOM-based lithofacies prediction

The accuracy of the trained SOM in Section 4.1 was verified through core description; therefore, we applied it to the entire 3D seismic dataset. The SOM-derived lithofacies sections intersecting wells L-30 and B-41 (Fig. 7) show a good delineation of the stratigraphic architecture and lateral facies variability across the study

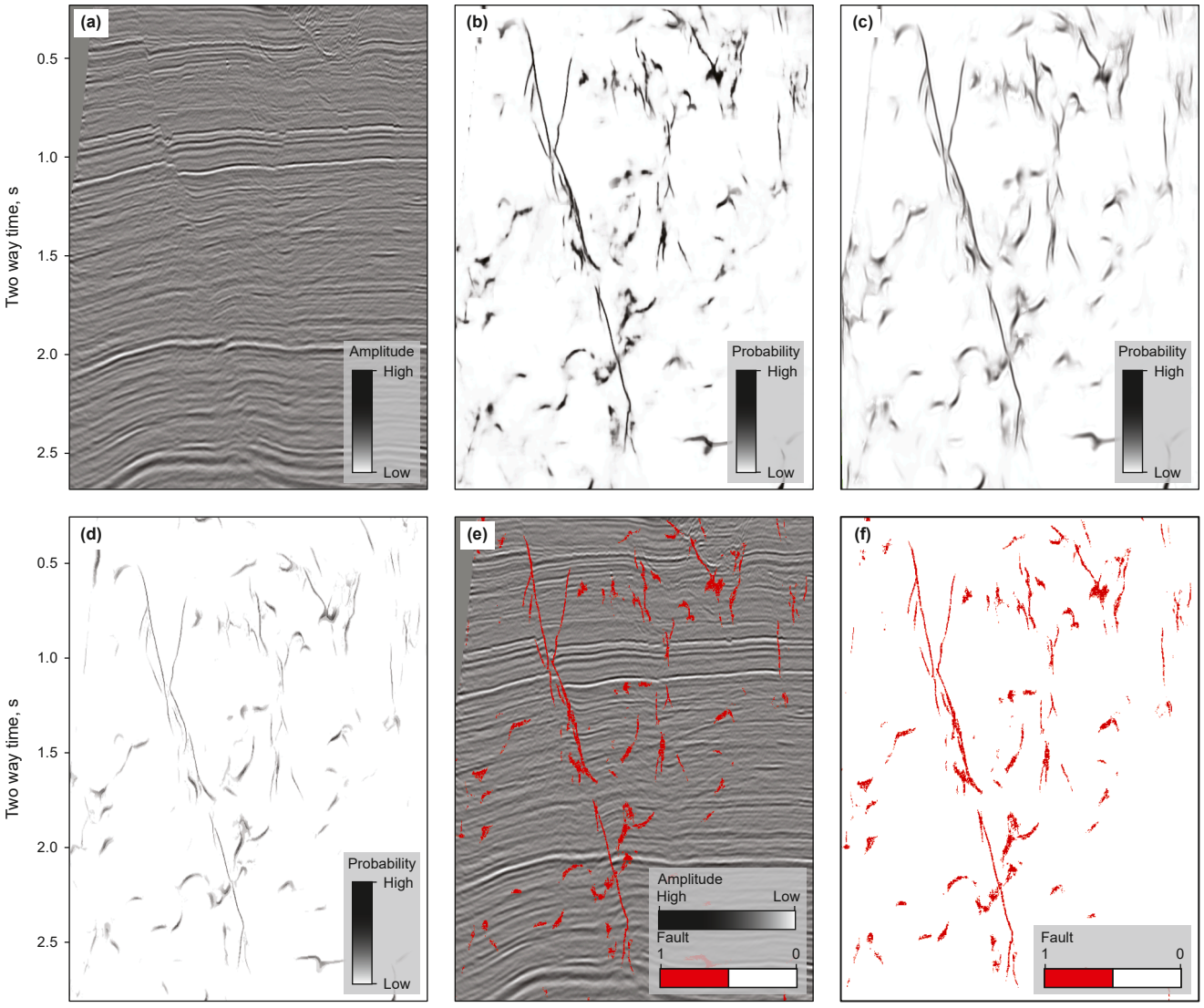



**Fig. 6.** Fault detection and seismic interpretation integration using CNN and SOM-based neuron clustering (Inline 1364). Top row: **(a)** Original post-stack seismic amplitude section; **(b)** CNN-based fault probability volume showing initial fault detection; **(c)** $LoG_{3D}$ enhanced fault probability volume with improved continuity and suppression of noise artifacts. Bottom row: **(d)** Fault skeletonization using directional filtering and thresholding, highlighting fault lineaments; **(e)** Seismic section overlaid with "fault neurons" identified by Self-Organizing Maps (SOMs), capturing localized discontinuities aligned with DL probabilities; **(f)** Isolated fault neuron clusters extracted from the full SOM classification volume, representing fault-related seismic responses.

**Table 4**
Input volumes serve as input attributes for SOM classification, enabling the representation of detected faults and their isolation as clustered fault neurons.

| Input attribute volume | Feature type | Extraction/processing step | Role in SOM fault-neuron isolation |
|---|---|---|---|
| CNN fault-probability volume | Structural fault attribute | Generated from the pre-trained CNN fault-detection workflow during seismic pre-processing. | Represents the primary fault-sensitive attribute. It highlights discontinuities, reflector offsets, and fault-like zones and provides the dominant structural control on fault-neuron clustering. |
| Skeletonized fault-probability volume | Structural fault attribute | Derived from the CNN fault-probability volume through post-processing and skeletonization. | Enhances the geometric continuity and centerline expression of detected faults, helping the SOM isolate narrow, fault-focused neuron responses. |
| SOM stratigraphic classification volume | Stratigraphic/seismic facies attribute | Produced from the independent stratigraphic SOM analysis of seismic attribute patterns. | Provides stratigraphic context to distinguish fault-related neurons from non-fault stratigraphic or facies-related discontinuities. |

interval within the field. According to the PDF overlap analysis (Fig. S7), lithofacies predictions are most confident along major reservoir intervals, notably within the Upper and Lower Missisauga, where condensate sands (red) and water sands (cyan) exhibit lateral continuity and clear differentiation from non-reservoir facies. The SOM-classified facies, calibrated with petrophysical data and validated through statistical PDF overlap, delineate a coherent stratigraphic framework aligned with key seismic markers. The distinguished lithofacies are consistently linked across the fault plane for each stratigraphic level.

To improve the interpretability of the SOM lithofacies workflow, a feature-importance analysis was performed using the 24 retained seismic attributes (Fig. S8-10). This analysis was designed to complement the previous MI and PCA-based attribute-selection procedure by identifying which retained attributes contributed most strongly to SOM lithofacies separation. The global feature-

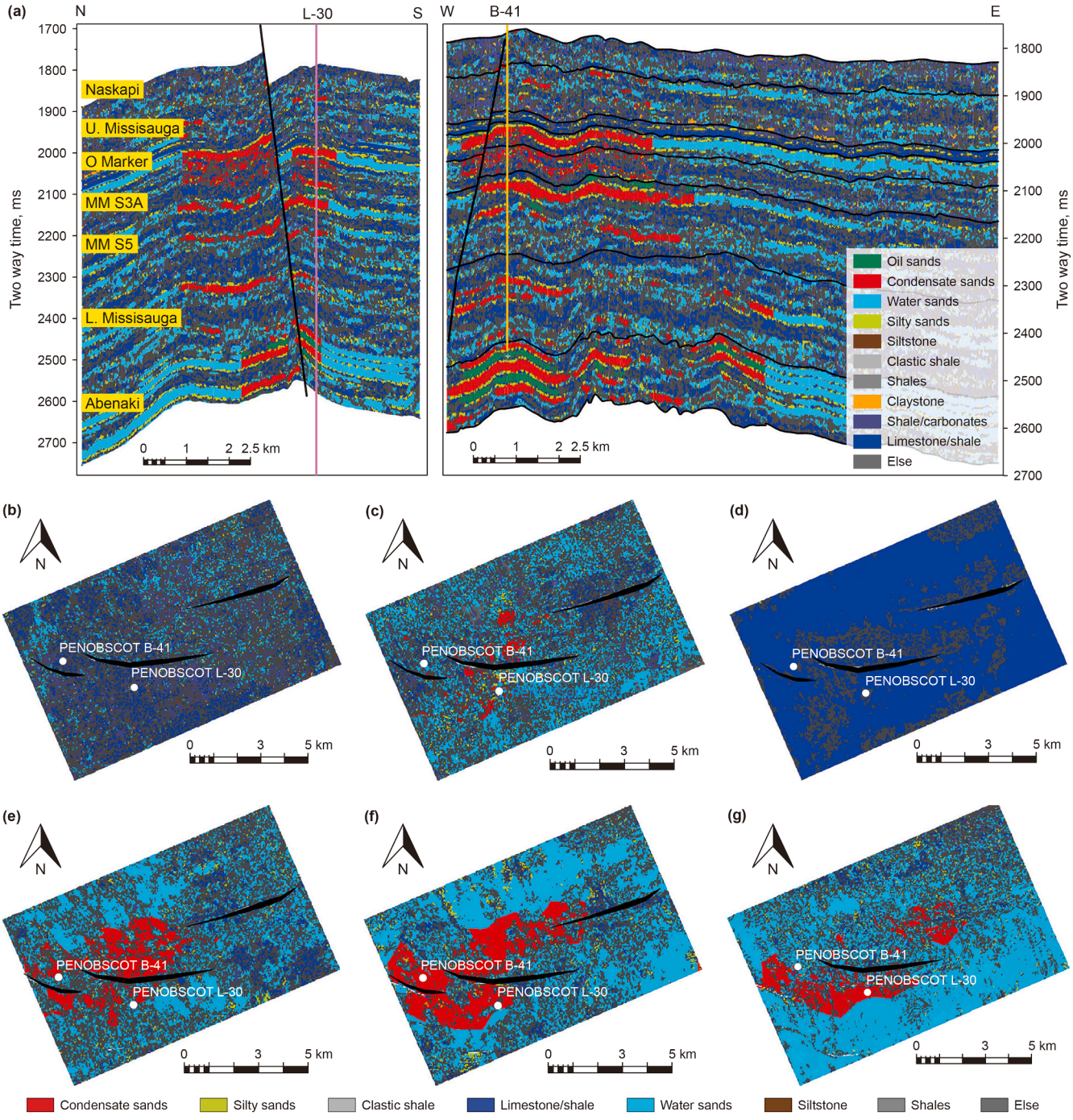



**Fig. 7.** SOM-driven lithofacies characterization integrating vertical sections and horizon maps. **(a)** 2D SOM-derived lithofacies sections intersecting wells L-30 and B-41, where the colored facies overlay is obtained from SOM neuron classification calibrated to lithofacies using petrophysical cutoffs and statistical PDF overlap with well log responses. **(b to g)** Plan-view SOM-classified lithofacies maps at six stratigraphic levels showing the structural framework at key horizons: **(b)** Naskapi; **(c)** Upper Missisauga S1; **(d)** O Marker; **(e)** Middle Missisauga S1; **(f)** Middle Missisauga S5; and **(g)** interval between the Lower Missisauga and Abenaki Formation. Facies classes include Condensate Sands (red), Water Sands (cyan), Silty-sands, Siltstone, and shale-dominated facies.

importance ranking shows that the dominant contributions come from spectral-decomposition attributes (Fig. S8), particularly ME spectral voice, CWT spectral magnitude, CWT spectral voice, and ME spectral magnitude attributes. The attribute-family summary indicates that ME spectral voice contributes approximately 35.4% of the total attribute-family influence (Fig. S9), followed by CWT spectral magnitude at 20.1%, CWT spectral voice at 16.7%, and ME spectral magnitude at 14.7%. Envelope amplitude, base seismic amplitude, thin-bed response, and instantaneous Q provide smaller but complementary contributions.

The facies-specific feature-importance heatmap further demonstrates that different lithofacies are controlled by different attribute combinations (Fig. S10). Shale-rich facies show stronger dependence on selected low-frequency spectral voice and magnitude attributes, reflecting differences in seismic texture and impedance response. Hydrocarbon-bearing sand classes, including Sand G1 – Light Oil and Sand G2 – Condensate, are mainly influenced by CWT and ME spectral attributes across multiple frequency bands, indicating that their separation is controlled by frequency-dependent amplitude and tuning behavior rather than by a single amplitude attribute. In contrast, Sand G3 – Water/Shaly shows a strong contribution from the thin-bed response attribute, suggesting that thin-bed tuning and internal heterogeneity are important for distinguishing these facies from cleaner hydrocarbon-bearing sands. These results show that the SOM lithofacies separation is physically interpretable and primarily controlled by frequency-dependent seismic responses linked to lithology, fluid content, and vertical heterogeneity.

Reservoir-prone facies, primarily represented by oil sands and condensate sands, are predominantly distributed within the Middle–Lower Missisauga and Abenaki formations (Fig. 8). These sand-prone intervals are particularly well developed around the Middle Missisauga S3A and Middle Missisauga S5 zones (Fig. 8b). The observed facies transitions suggest varying depositional energy and a potential combination of stratigraphic and structural trapping configurations. Water sands appear intercalated with hydrocarbon-bearing units. Above and between these reservoir intervals, the presence of regionally continuous clastic shale, shale/carbonate, and claystone facies suggests effective vertical sealing and baffle mechanisms, supporting reservoir compartmentalization. The Abenaki interval, although more heterogeneous, exhibits a basal transition from thick carbonate to shale. While the mic-mac sands exhibited a good hydrocarbon presence, the SOM did not delineate the baffles and showed continuous gas and oil-bearing sands. The thicknesses of the stratigraphic units and the delineated lithologies show minimal variations, suggesting post-depositional deformation. The preservation of stratigraphic layering across these flexures implies a dominantly stratigraphic rather than structural control on reservoir geometry. This illustrates SOM's capability to classify and capture key stratigraphic patterns and lithological transitions with high fidelity, demonstrating its robustness in resolving fine-scale heterogeneities critical for reservoir characterization and modeling.

### 5.2. Fault detection

We applied a CNN-SOM hybrid classification workflow, as shown in Fig. 5, to generate high-resolution fault probability volumes and identify fault-related geobodies. Fig. S13 presents a 3D volume display of the seismic amplitude data, integrated with fault geobodies identified from CNN-derived fault probability volumes and refined via SOM clustering. The amplitude volume provides stratigraphic context, while the superimposed fault geobodies delineate a network of structurally coherent discontinuities. The 3D visualization enhances spatial interpretation by enabling a comprehensive understanding of the reflector architecture's vertical and lateral continuity.

The CNN fault model used in this study was applied to the present dataset in inference mode without additional fine-tuning on dataset-specific fault labels. This may introduce a potential domain-shift limitation, as seismic surveys may differ in signal-to-noise ratio, dominant frequency, processing workflow, reflector continuity, and fault-imaging character. Therefore, the CNN-derived fault-probability volume is introduced here as a fault-enhancement product rather than a standalone deterministic fault interpretation. To evaluate the generalization behavior of the pre-trained model within the Penobscot survey, a limited manual validation test was performed on representative inline/crossline sections (Figs. 9, S14). Faults and discontinuities were manually interpreted from seismic amplitude sections and converted into reference binary masks (Fig. 9a). These masks were compared with thresholder CNN-derived fault-probability predictions using precision, F1-score, AUC, optimized thresholded analysis, and point-to-surface distance statistics (Fig. 9b). The validation results indicate that the pre-trained U-Net model captures the main manually interpreted fault trends, but its performance varies between sections. Precision values range from approximately 0.66 to 0.76, while standard-threshold F1-scores range from approximately 0.56 to 0.82. After threshold optimization, F1-scores improve to approximately 0.75 to 0.95, with optimal thresholds of approximately 0.91 to 0.93 (Table 5). This suggests that the CNN model produces useful fault-probability responses (Fig. 9c), but that higher confidence thresholds are required to suppress weak false-positive detections in the Penobscot survey. The point-to-surface distance analysis shows mean distances of approximately 2.06-2.49 pixels and median distances of approximately 1.00-1.44

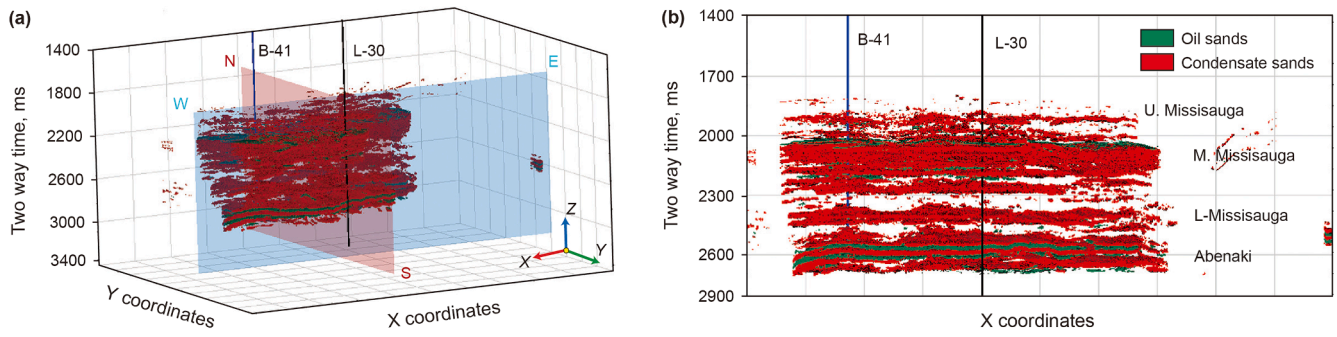



**Fig. 8.** A 3D perspective view of reservoir-prone SOM-classified lithofacies across the Penobscot Field. Wells B-41 and L-30 are shown at their intersection locations. **(a)** Southwestern view showing the intersections displayed in Fig. 7. **(b)** Southern 3D view showing multiple vertically stacked reservoir-prone intervals.

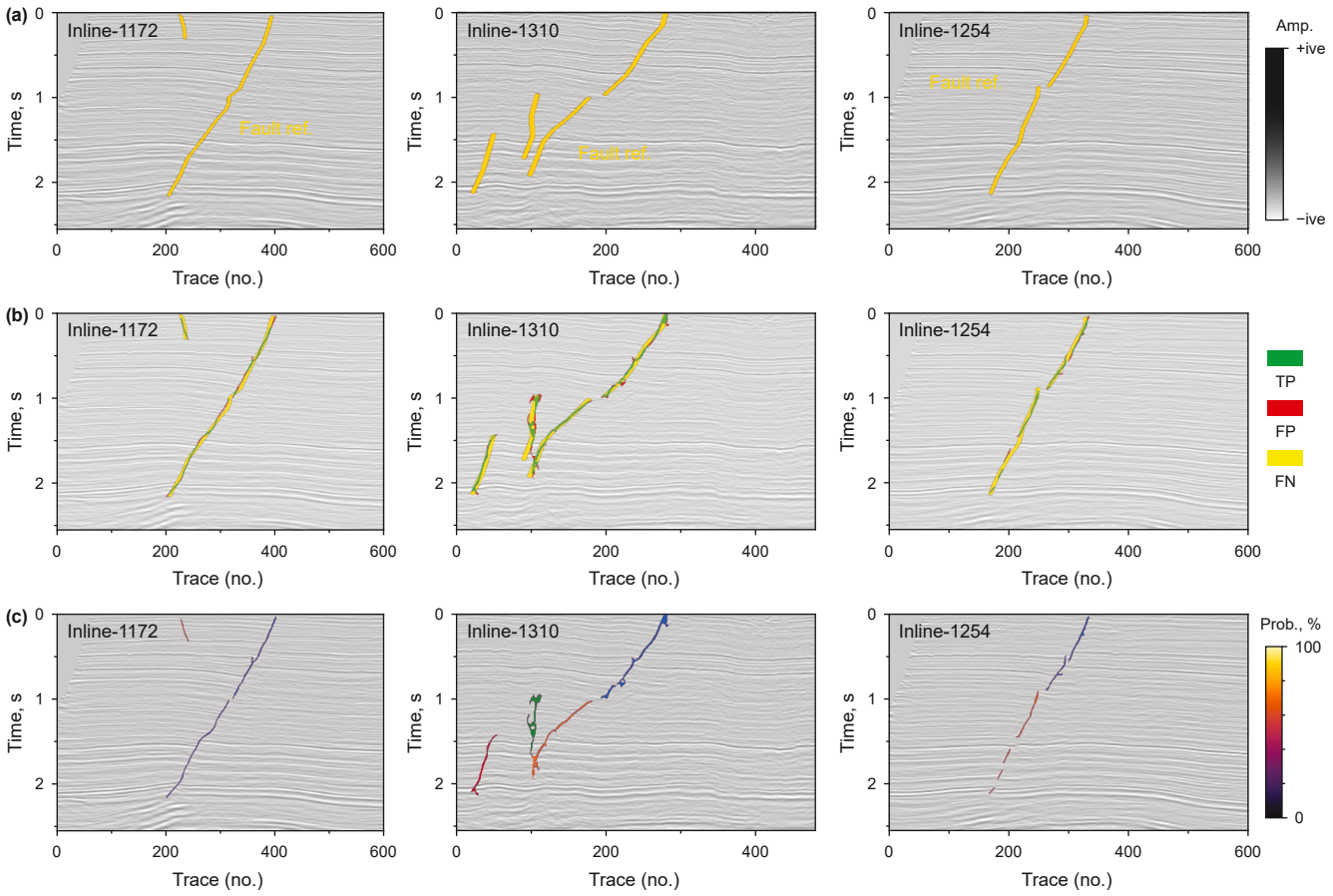



**Fig. 9.** Fault-detection comparison for representative seismic inlines. **(a)** Reference fault interpretations. **(b)** Pixel-wise classification of detected faults as true positives (TP), false positives (FP), and false negatives (FN) relative to the reference labels. **(c)** Extracted fault-probability traces.

pixels, indicating close spatial agreement between the predicted and manually interpreted fault traces where detections occur (Fig. S14).

Major fault planes appear as vertically aligned low-continuity regions that intersect both inline and crossline panels, with corresponding horizon offsets clearly visible (Fig. 10 and Fig. S13). The positioning of wells L-30 and B-41 relative to these fault planes confirms previously mapped fault trends and indicates zones of potential compartmentalization. Furthermore, the visualization supports geologic consistency with regional fault trends characterized by NE–SW extensional patterns and reveals previously unresolved fault splays, demonstrating the added interpretive value of combining machine-learning-based structural detection with stratigraphic SOM classification. Several prominent fault planes are observable as vertical reflector terminations and amplitude discontinuities, particularly between 2200 and 2600 ms TWT. The most significant fault cuts through the O Marker and Middle Missisauga S3A horizons, suggesting a long period of extensional features. Well B-41 intersects this fault zone directly, reinforcing previous interpretations that lie within a structurally active compartment. In contrast, L-30 appears more stratigraphically continuous, yet is bounded by plays visible on the inline section.

Fault trace maps extracted from the CNN-SOM classification volume at selected time slices are shown in Fig. 10b–d. The black lines represent fault skeletons projected onto horizontal slices, with B-41 and L-30 indicated for spatial reference. The faults exhibit a consistent E–W trend, aligning with the regional tectonic fabric associated with salt-influenced extensional deformation. Fault complexity increases with depth, as evident in the denser fracture network at 2500 ms, which consists of two families of fractures trending E-W and N-S. This depth-dependent variation highlights the reactivation of pre-existing structures within deeper Missisauga and Abenaki units consistent with

**Table 5**
Quantitative fault-detection performance for representative seismic inlines. Metrics include precision, specificity, AUC, tolerance-based F1 scores at 3, 5, and 10 pixels, and orientation consistency, with average values reported across all evaluated inlines.

| Inline | Precision | Specificity | AUC | F1-3px | F1-5px | F1-10px | Orient Con. |
|---|---|---|---|---|---|---|---|
| 1310 | 0.75 | 1.00 | 0.66 | 0.82 | 0.95 | 0.99 | 0.91 |
| 1172 | 0.66 | 1.00 | 0.62 | 0.60 | 0.82 | 1.00 | 0.92 |
| 1254 | 0.76 | 1.00 | 0.65 | 0.59 | 0.75 | 0.90 | 0.92 |
| Average | 0.72 | 1.00 | 0.64 | 0.67 | 0.84 | 0.96 | 0.92 |

Precision = positive predictive value; Specificity = true negative rate; AUC = area under the receiver operating characteristic curve; F1-3px, F1-5px, and F1-10px = F1 score computed using 3-, 5-, and 10-pixel spatial matching tolerances; Orient Con. = orientation consistency.

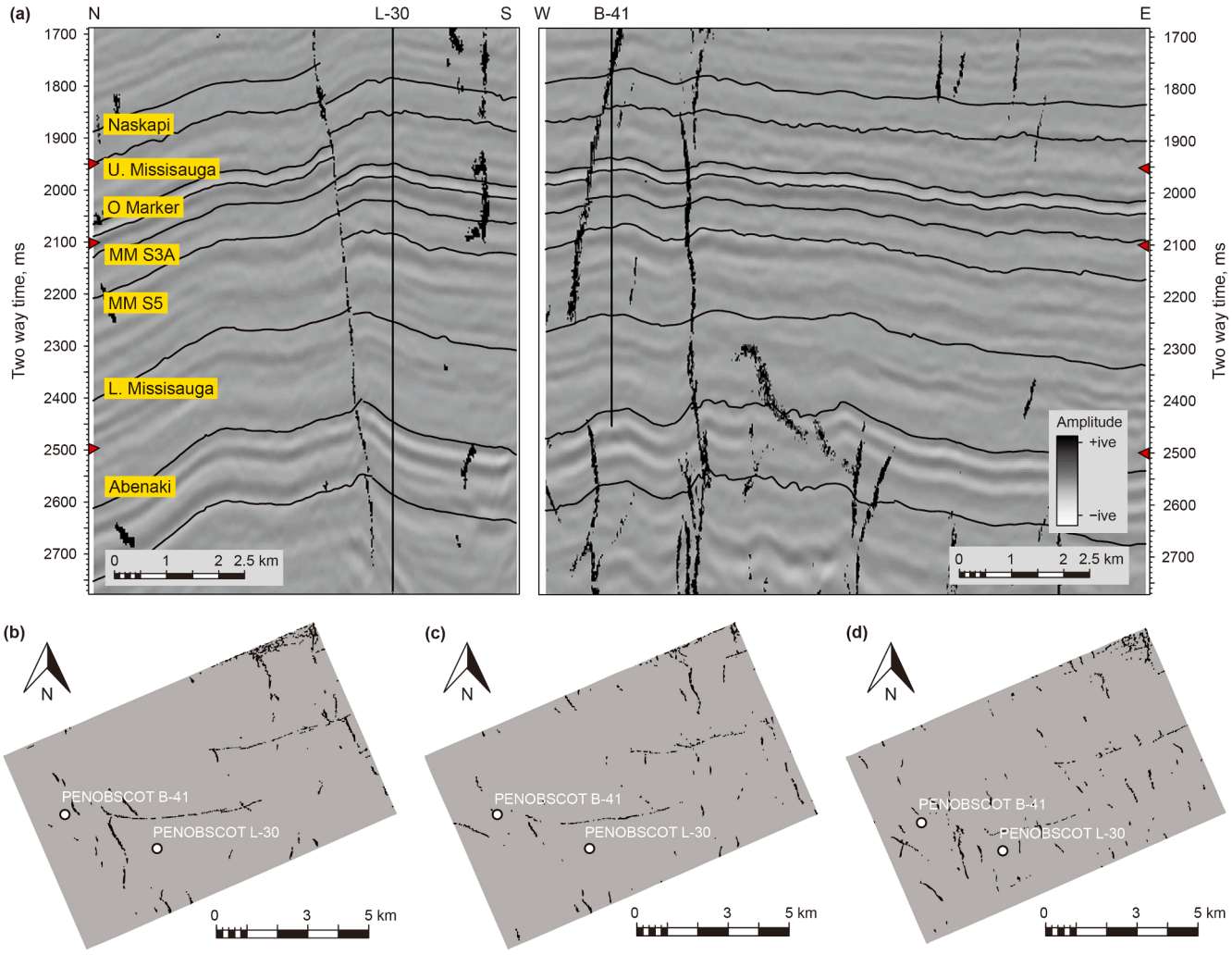



**Fig. 10.** Integrated seismic interpretation and fault skeleton analysis from CNN–SOM workflows. **(a)** Vertical seismic sections intersecting wells L-30 (left) and B-41 (right), displaying key predicted stratigraphic horizons from the Naskapi to the Abenaki Formation. Red arrows mark the two-way travel times of extracted seismic time slices used for fault analysis at 1950 ms, 2100 ms, and 2500 ms. Black linear discontinuities correspond to fault planes delineated by CNN-derived skeletons and isolated through SOM-based fault neuron classification. **(b to d)** Fault skeleton time slices extracted from the CNN–SOM hybrid volume at **(b)** 1950 ms (Upper Missisauga), **(c)** 2100 ms (Middle Missisauga), and **(d)** 2500 ms (Abenaki Formation). Fault networks increase in density and structural complexity with depth and exhibit consistent E-W and N-S-oriented fault trends.

interpretations of basement-involved faulting. The spatial distribution of fault traces, combined with their stratigraphic alignment, demonstrates the CNN-SOM framework's ability to resolve fault connectivity and compartmentalization across key reservoir intervals. The segmentation of faults into distinct clusters (SOM's fault neurons) enables a more interpretable rendering of structural elements, allowing a better, unbiased interpretation and delineation of the faults and fractures network. The predicted fault directions reveal a predominantly E-W trend with local bifurcations and play suggestive of synthetic and antithetic faulting. These faults likely formed during early extension and were subsequently influenced by multiple tectonic episodes. Wells B-41 and L-30 penetrate proximally into high-contrast zones, supporting the interpretation that these faults influence both reservoir distribution and potential fluid-migration pathways.

The outcome of multi-attribute seismic analysis on a representative time slice at 2500 ms within the Abenaki Formation is presented in Fig. 11. The Sobel-filtered similarity attribute reveals a well-defined network of E-W- and N-S-striking discontinuities, indicative of faulting patterns associated with Jurassic rifting and possibly salt-related deformation. These faults are further corroborated by high values of curvedness and strike curvature (K2), delineating zones of fault drag and structural flexure. Dip azimuth and dip magnitude attributes confirm fault-induced deformation, showing consistent rotational trends along fault corridors and enhanced dip values across major discontinuities. The integration of dip-azimuth overlays with dip-magnitude highlights the presence of low-angle normal faults that offset large structural blocks. The spatial alignment of these fault zones with lithofacies discontinuities, previously identified through SOM classification, supports their role in stratigraphic compartmentalization and fluid migration. This confirms the effectiveness of the hybrid CNN-SOM approach in resolving both major and subordinate fault geometries, thereby enhancing the structural interpretation across the studied intervals. The extracted faults exhibit a strong alignment with regional E-W trends, which are linked to regional tectonics and previous work.

### 5.3. *Integration of fault detection and SOM lithofacies classification*

One of the key outcomes of this study is the integration of CNN-based fault probability volumes and post-processed, skeletonized

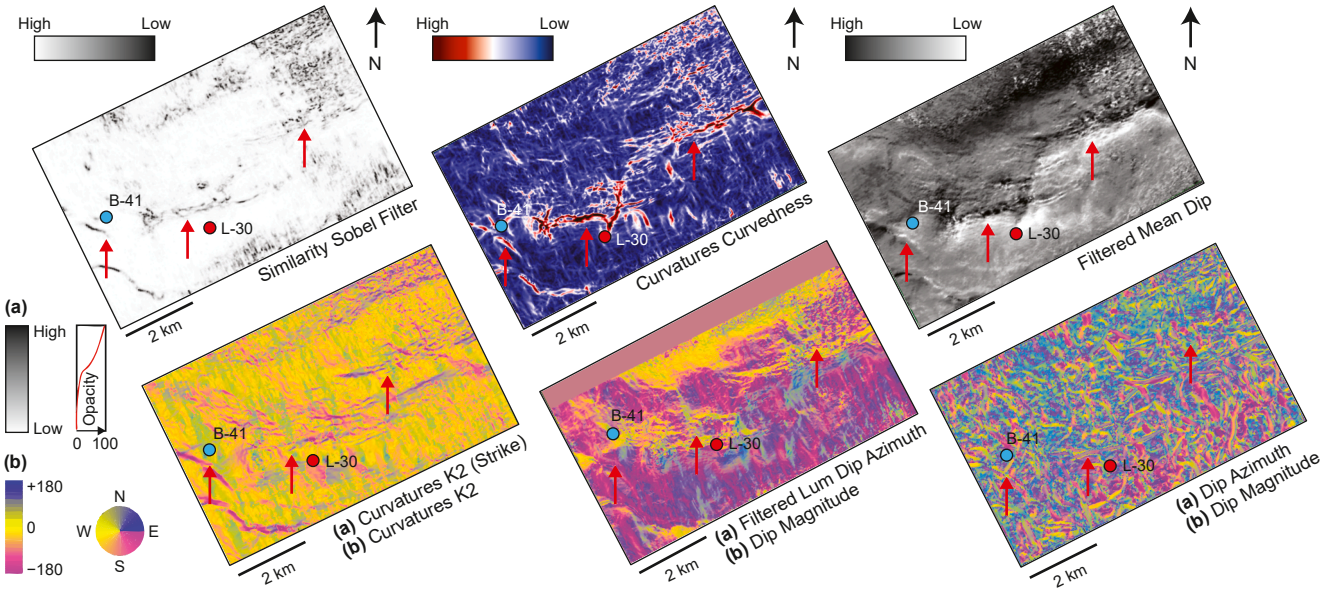



**Fig. 11.** Structural seismic attribute slices at 2500 ms within the Abenaki Formation, surrounding wells B-41 (blue) and L-30 (red), in the Penobscot Field. Shown attributes include similarity Sobel filter, curvedness curvature, filtered mean dip, strike curvature (K2), filtered Lum dip azimuth and magnitude, and dip azimuth and dip magnitude. Red arrows indicate major fault structures.

fault volumes with SOM lithofacies classification. This structural-stratigraphic approach enhances seismic interpretation by isolating fault-related neurons, referred to as fault neurons, which delineate structural discontinuities while preserving stratigraphic integrity (Mora et al., 2022a). As shown in Fig. 10, incorporating fault attributes into the SOM training process enables identification of discontinuous fault segments, consistent with CNN-derived trends, but now embedded within the broader lithological framework. This link between data-driven structural delineation and unsupervised facies classification enables interpreters to visualize fault planes as amplitude discontinuities and to tie structural features to lithofacies changes and compartment boundaries. Moreover, the results demonstrate that the SOM was able to resolve distinct neuron clusters associated with fault corridors, thereby enhancing the resolution of fracture zones and contributing to a more comprehensive understanding of reservoir compartmentalization (Roden et al., 2015; Zhao and Mukhopadhyay, 2018). A sequence of SOM-classified horizon maps extracted from six stratigraphic intervals within the 1900–2500 ms time window is illustrated in Fig. 7b–g. These horizons collectively demonstrate the capability of unsupervised learning to reveal subtle lithofacies transitions, resolve sub-seismic heterogeneities, and delineate stratigraphically controlled HACs that are often obscured using traditional amplitude-based interpretation.

In these maps, Condensate Sands (red) and Water Sands (cyan) are observed as dominant lithologies. Their lateral continuity and spatial confinement suggest depositional control is likely governed by deltaic distributary channels and slope-channel-levee systems derived from the progradational Sable Delta. The consistent E-W orientation of sand-rich facies corresponds well with known sediment transport directions in the region. Notably, these SOM maps enable interpreters to track the termination and segmentation of sand bodies at a sample-by-sample resolution, eliminating the need for interpolation, and making them particularly suited for delineating pinch-outs, facies boundaries, and thin stratigraphic traps.

Using direct mapping of SOM neuron outputs, which provides high-resolution patterns, we successfully tracked the development of condensate-rich sand around the Penobscot B-41 and L-30 wells, including channel-like and lens-shaped geometries. The presence of silty sands and siltstones (olive and brown), particularly along the flanks of the reservoir-prone intervals, suggests potential barriers or internal heterogeneities. These facies are likely to influence permeability distribution and sweep efficiency, and their delineation using SOM is critical for dynamic reservoir modeling. Importantly, the maps indicate that shales and clastic shales form effective lateral and vertical seals, thereby enhancing the interpretability of DHIs as HACs rather than mere amplitude anomalies.

## 6. Discussion

### 6.1. Spectral attribute optimization for lithofacies classification

To evaluate the seismic expression of the eight SOM-derived lithofacies and their planar distribution (Fig. 7), we analyze the relationship between optimized seismic attributes and lithofacies classes, linking attribute behavior to depositional and structural controls. To assess statistical dependency, redundancy, and information content among the 24 selected seismic attributes, a comprehensive multi-metric dependency analysis was conducted using Pearson correlation, Spearman rank correlation, and Mutual Information (MI), following the framework of Kim et al. (2019) and summarized in Table S3. This strategy extends beyond simple correlation screening by explicitly preserving geologically meaningful, nonlinear, and nonmonotonic attribute relationships that are often suppressed in amplitude-centric analyses.

The integration of PCA-based dimensionality reduction with MI-driven attribute prioritization mitigates the curse of dimensionality while avoiding the bias of variance-dominated feature ranking inherent to PCA alone. Attributes exhibiting high MI values (MI > 6) but weak linear correlation, such as SD CWT magnitude and voice components at 35 Hz, were retained because they encode nonlinear geological responses associated with thin-bed tuning and fluid-sensitive interference effects. High-frequency spectral attributes (75–85 Hz) proved particularly diagnostic for distinguishing lithofacies transitions below classical tuning

thickness, a regime where broadband seismic attributes commonly fail.

Correlation analysis between seismic attributes and SOM-derived lithofacies reveals distinct seismic response patterns across the eight classes. Reservoir-prone facies, including oil sands and condensate sands, are characterized by elevated high-frequency spectral magnitudes, enhanced envelope responses, and localized instantaneous-frequency anomalies, consistent with porous, hydrocarbon-filled intervals exhibiting resonance effects. In contrast, shale-, claystone-, and limestone-dominated facies display subdued high-frequency responses and smoother amplitude envelopes, reflecting lower impedance contrasts and reduced tuning sensitivity. These attribute–facies relationships confirm that lithofacies separation is driven by multi-attribute seismic behavior rather than single-attribute thresholds.

For example, SD Maximum Entropy spectral magnitude and voice components at 75–85 Hz capture complementary phase–amplitude variations that enhance discrimination of thinly interbedded clastic–carbonate successions (Fig. S10). This attribute sensitivity is quantitatively supported by the SOM classification performance (Fig. S12a–b), where recall reaches 1.00 for limestone/shale, oil sands (Sand G1), and condensate sands (Sand G2), indicating complete retrieval of true lithofacies samples. The normalized confusion matrix further shows perfect classification of Sand G1 (100%), while Sand G2 is correctly identified in 83% of cases, with limited misclassification (17%) into limestone/shale facies, reflecting expected spectral overlap in transitional depositional settings rather than algorithmic instability. The lower precision observed for limestone/shale (0.50) is consistent with facies mixing at sand–carbonate interfaces and highlights the conservative nature of the unsupervised classification.

The planar distribution of lithofacies (Fig. 7) further reflects the combined influence of depositional architecture and structural compartmentalization. Condensate and water-bearing sands exhibit laterally continuous yet structurally segmented patterns, controlled by fault-related compartment boundaries and sediment-routing pathways within the Missisauga and Abenaki formations. Non-reservoir facies form regionally extensive sealing units that bound reservoir clusters both laterally and vertically. These spatial patterns demonstrate that lithofacies continuity is governed by the interaction of depositional processes and fault-controlled segmentation rather than by stratigraphy alone.

SOM training convergence behavior (Fig. S6) indicates that neuron weight stabilization occurs after mid-epoch training, during which the network resolves subtle but persistent spectral differences between clastic shales, silty sands, and carbonate-rich intervals. This convergence behavior reflects effective sampling of the optimized attribute space rather than sensitivity to specific SOM hyperparameters. Distinct neuron classes are particularly evident in stratigraphic units SU-4 and SU-5 of the Penobscot L-30 well (Fig. 12), where high-frequency spectral dominance coincides with favorable petrophysical indicators of reservoir quality ($\varnothing_e$ >15%, low $S_w$, and low *GR*).

Overall, this analysis demonstrates that MI-guided spectral attribute optimization, combined with SOM-based unsupervised learning, provides a robust alternative to conventional amplitude-driven or single-method clustering approaches. By emphasizing nonlinear seismic responses and topology-preserving classification, the proposed workflow enhances lithofacies discrimination, supports the identification of Hydrocarbon Anomaly Clusters (HACs), and improves geological interpretability in heterogeneous, structurally complex reservoirs.

### 6.2. Petrophysical validation of SOM-lithofacies

The SOM's voxel-wise classification operating at seismic sample resolution (4 ms ≈ 8 m) yielded a high-fidelity lithofacies framework validated against core and logs (Fig. 12). Seven stratigraphic units (SU-1 to SU-7) were resolved, each corresponding to seismic reflectors characterized by high continuity and amplitude anomalies, suggesting potential hydrocarbon accumulations. The vertical facies progression from sand-prone deposits in the lower units to more shale-rich intervals upward reflects compensational stacking and retrogradational parasequences typical of passive margin shelf systems (Asim et al., 2016; Cummings et al., 2006; Straub et al., 2009). The SOM's ability to resolve these stratigraphic trends highlights its sensitivity to depositional architecture and subtle variations in seismic attributes.

Units SU-1 through SU-3 exhibit favorable reservoir properties, with low *GR* (<70 gAPI), high $\varnothing_e$ (≥15%), and low $S_w$ < 60%, aligning with SOM neuron clusters corresponding to oil- and condensate-saturated sands. Specifically, SU-1 and SU-3 are associated with Hydrocarbon Anomaly Clusters HAC-1 and HAC-3, respectively, both of which represent condensate-bearing sands characterized by elevated seismic amplitudes, low $V_{sh}$, and low $S_w$. SU-2 defines HAC-2, comprising oil-saturated sands identified by lower amplitudes but similarly low $V_{sh}$, and $S_w$ values. In contrast, SU-6 and portions of SU-7 are dominated by higher *GR* and $V_{sh}$ values and reduced $\varnothing_e$, consistent with neuron clusters classified as clastic shale or carbonate-shale facies. This correspondence between SOM neuron classes and petrophysical facies confirms the model's capability to capture lithological and fluid variations (Figs. 7 and 8). Furthermore, it demonstrates how SOM-based classifications trained on multi-attribute seismic data can resolve sub-seismic features and complex facies architectures more effectively than conventional amplitude-based methods (Chenin, 2020; Roden et al., 2015).

This voxel-wise classification allows high-resolution mapping of features even below the tuning thickness. For example, the siliciclastic units (SU1 to SU7) in the seismic cross-section (Fig. 12a and b) are differentiated in the SOM-facies logs (Fig. 12c), with each neuron color corresponding to a petrophysical lithofacies class derived from the well logs. These classes encompass reservoir facies (oil sands, condensate sands, and water sands) and non-reservoir facies (shales, limestone/shale, and siltstone), providing an intuitive topological map of geologically meaningful units. Importantly, the correspondence between SOM neurons and petrophysical properties, including *GR*, $\varnothing_e$, $S_w$, and $V_{sh}$, enables direct facies prediction (Rashid et al., 2022). In several depth intervals, condensate-bearing sands (Low *GR*, low $S_w$, low $V_{sh}$) are identified by discrete SOM neuron classes not resolved in the original seismic amplitude data. The well-calibrated SOM output confirms several lithofacies transitions across sequence boundaries SU-1 through SU-7, with facies boundaries captured even in low-reflectivity zones (e.g., SU-6 and SU-4). These patterns, derived from unsupervised learning, align well with trends in *GR*, $\varnothing_e$, and $S_w$ logs, validating the interpretability and geological relevance of the SOM neurons. This capability to map fluid contacts and facies boundaries without interpolation surpasses conventional methods, enabling the detection of pinch-outs and stratigraphic traps at the sample scale. The direct neuron-to-petrophysics linkage demonstrates the utility of SOM as a quantitative tool for seismic-driven reservoir characterization, thereby reducing reliance on subjective amplitude interpretation.

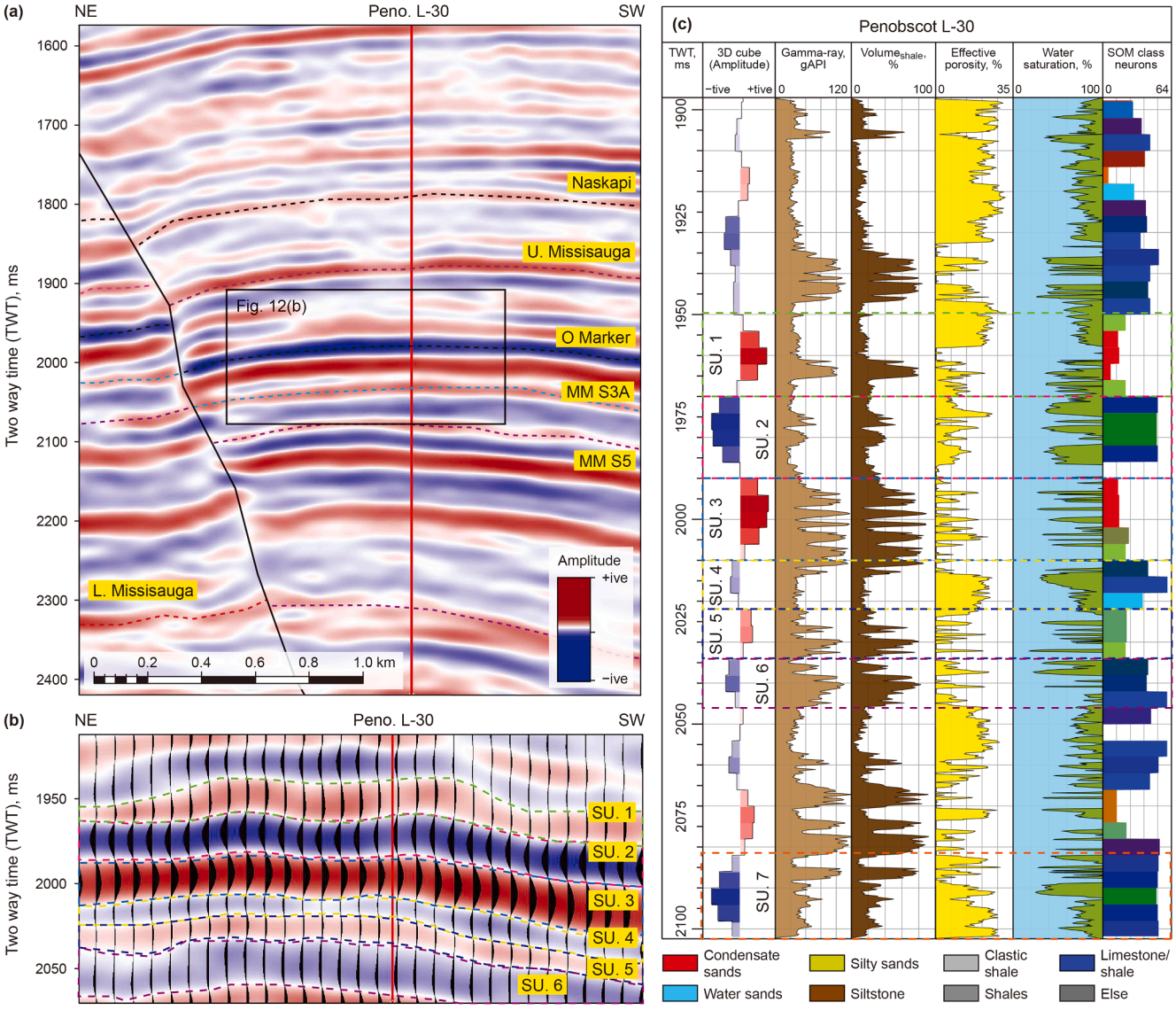



**Fig. 12.** **(a)** Inline seismic section showing amplitude variations and key stratigraphic horizons, including the Naskapi, Upper Missisauga, O Marker, and Lower Missisauga units. **(b)** Zoomed-in section highlighting sequence boundaries (SU-1 to SU-7) and lateral amplitude continuity across the L-30 well trajectory. **(c)** Well log data from L-30, including amplitude, *GR*, $V_{sh}$, $\varnothing_e$, $S_w$, and SOM neuron classification.

### 6.3. Uncertainty and future work

Despite the high-resolution lithofacies classification achieved using SOMs integrated with multi-attribute data, petrophysical constraints, and fault interpretation, several sources of uncertainty remain and require careful consideration. Pre-stack angle-dependent attributes (e.g., AVA) could enhance fluid discrimination near contacts (Provenzano et al., 2017; Swisi, 2009), potentially underrepresenting subtle fluid signatures, especially near condensate-sand-water contacts or thin-bed reservoirs, such as those observed in the Upper Missisauga interval. While attribute selection was optimized using PCA, mutual information, and correlation analysis, inherent subjectivity remains in choosing which features to include, and high inter-attribute redundancy may overshadow less dominant but geologically significant signals. Furthermore, petrophysical facies calibration was based primarily on two wells (L-30 and B-41), which may not fully capture lateral variability across the field, especially in zones of shale-draped channel pinch-outs or silty sand incursions.

Broadband spectral attributes successfully enhanced the resolution of thin beds and HACs, but their high-frequency sensitivity also introduces susceptibility to tuning artifacts and noise, potentially leading to local misclassifications. Developing probabilistic SOMs could enable the visualization of uncertainty and the mapping of confidence in lithofacies boundaries. The result provides a richer understanding of the reservoir system, enabling interpreters to connect seismic expression, facies architecture, and field-scale development strategies. However, generalizability should be tested in deltaic or salt-free settings via transfer learning, integrating probabilistic SOMs to quantify classification uncertainty, incorporating rock physics inversions into meta-seismic attributes with elastic properties, and extending HACs to 4D seismic for dynamic reservoir monitoring. These advancements will transition ML-driven interpretation from static to dynamic facies mapping and predictive reservoir modeling.

## 7. Conclusions

This work provides an integrated workflow in which SOM-based unsupervised learning and CNN-derived fault attributes jointly improve the interpretation of stratigraphic heterogeneity and structural compartmentalization at seismic-sample scale. The integration of SOM-based seismic facies classification with CNN-derived fault detection, petrophysical calibration, and attribute optimization in the Penobscot field, Scotian Basin, offshore Canada, led to the following findings:

- The application of an 8×8 hexagonal SOM applied on ~596,827 seismic samples enabled the robust classification of lithofacies tied to petrophysical indicators (*GR*, $V_{sh}$, $S_w$, and $\varnothing_e$), effectively delineating reservoir units including oil-, condensate-, and water-saturated sands at three key stratigraphic levels, providing unbiased seismic-based delineation of hydrocarbon potential
- SOM has successfully differentiated sealing/reservoir units at high resolution, showing multiple reservoirs vertically stacked, solving the geological complexity of the field.
- The field architecture aligns with NE-SW-trending low-relief anticlines intersected by E-W normal faults, and hydrocarbons appear to have high-quality thick reservoirs toward mid-Missisauga with high hydrocarbon potential and thick continuous lateral seals overlying the reservoir sequence.
- Fault and fractures prediction, derived from CNN-based fault probability volumes, has successfully highlighted fault locations accurately correlating with the regional tectonic setting and previous manual interpretation.
- This work establishes a new paradigm for reservoir characterization, where unsupervised learning (SOM) and deep learning (CNN) converge to quantify stratigraphic complexity and structural integrity at unprecedented resolution. Future applications will extend this workflow to pre-stack domains and time-lapse seismic, enabling dynamic reservoir management.

## CRediT authorship contribution statement

**Tarek Khalifa:** Writing – original draft, Software, Methodology, Investigation, Formal analysis, Conceptualization. **Ahmed Eleslambouly:** Writing – review & editing, Writing – original draft, Visualization, Methodology, Formal analysis, Data curation, Conceptualization. **Gui-Bin Zhao:** Writing – review & editing, Visualization, Validation. **Amir Ismail:** Writing – review & editing, Validation, Software.

## Availability of data and materials

The dataset used in this work can be acquired from GSC (basin.marine-geo.canada.ca/wells/index_e.php), NSDE, and CNSOPB (cnsopbdigitaldata.ca/geoviewer/dmc), or TerraNubis (terranubis.com/datainfo/Penobscot).

## Declaration of competing interest

The authors declare that they have no known competing financial interests or personal relationships that could have appeared to influence the work reported in this paper.

## Acknowledgments

The authors sincerely express their gratitude to NSDE, CNSOPB, and TerraNubis for granting open access to the 3D seismic and well data. They also extend their appreciation to Geophysical Insight for the use of the Paradise software in the SOM analysis. Finally, we express our gratitude to the Fulbright Egypt Commission for awarding Tarek Khalifa a Master's scholarship to Texas A&M University-College Station.

## Supplementary data

Supplementary data to this article can be found online at https://doi.org/10.1016/j.petsci.2026.05.052.

## References

Abdelmaksoud, A., Ali, M.Y., 2024. Petroleum system analysis of Fujairah basin, eastern offshore of the United Arab Emirates. Mar. Petrol. Geol. 170, 107157. https://doi.org/10.1016/j.marpetgeo.2024.107157.

Ali, M., Ali, M.Y., Abdelhady, A., 2024. Cretaceous petroleum system elements in the Komombo Basin, Egypt. Pet. Geosci. 30 (4), 2024–2043. https://doi.org/10.1144/petgeo2024-043.

Ali, M., Zhu, P., Huolin, M., Jiang, R., Zhang, H., Ashraf, U., Hussain, W., 2025. Data-driven machine learning approaches for precise lithofacies identification in complex geological environments. Geo-Spatial Inf. Sci. 28 (4), 1722–1742. https://doi.org/10.1080/10095020.2024.2405635.

An, Y., Du, H., Ma, S., Niu, Y., Liu, D., Wang, J., Du, Y., Childs, C., Walsh, J., Dong, R., 2023. Current state and future directions for deep learning based automatic seismic fault interpretation: a systematic review. Earth Sci. Rev. 243, 104509. https://doi.org/10.1016/j.earscirev.2023.104509.

Ashraf, U., Zhang, H., Anees, A., Ali, M., Zhang, X., Shakeel Abbasi, S., Nasir Mangi, H., 2020. Controls on reservoir heterogeneity of a shallow-marine reservoir in Sawan Gas Field, SE Pakistan: implications for reservoir quality prediction using acoustic impedance inversion. Water 12 (11), 2972. https://doi.org/10.3390/w12112972.

Asim, S., Ahmad, S., Zhu, P., Naseer, M.T., Butt, M., 2016. Spectral decomposition application for analyzing the structure and the reservoir potential: a case study of Penobscot, Nova Scotia offshore, Canada. Arabian J. Geosci. 9, 1–20. https://doi.org/10.1007/s12517-015-2168-x.

Babikir, I., Elsaadany, M., Sajid, M., Laudon, C., 2022. Evaluation of principal component analysis for reducing seismic attributes dimensions: implication for supervised seismic facies classification of a fluvial reservoir from the Malay Basin, offshore Malaysia. J. Petrol. Sci. Eng. 217, 110911. https://doi.org/10.1016/j.petrol.2022.110911.

Barnes, A.E., 2016. Handbook of Poststack Seismic Attributes. Society of Exploration Geophysicists. https://doi.org/10.1190/1.9781560803324.

Bhatnagar, P., Bennett, C., Khoudaiberdiev, R., Lepard, S., Verma, S., 2017. Seismic attribute illumination of a synthetic transfer zone. SEG Technical Program Expanded Abstracts 2017, Society of Exploration Geophysicists 2112–2116. https://doi.org/10.1190/segam2017-17664850.1.

Brown, D., 2008. Regional Geology of the Scotian Basin. Canada-Nova Scotia Offshore Petroleum Board retrieved from. www.cnsopb.ns.ca/sites/default/files/resource/regional_geology_of_thescotianbasin-2008.pdf.

Campbell, D.C., Shimeld, J., Deptuck, M.E., Mosher, D.C., 2015a. Seismic stratigraphic framework and depositional history of a large Upper Cretaceous and Cenozoic depocenter off southwest Nova Scotia, Canada. Mar. Petrol. Geol. 65, 22–42. https://doi.org/10.1016/j.marpetgeo.2015.03.016.

Campbell, T.J., Richards, F.B., Silva, R.L., Wach, G., Eliuk, L., 2015b. Interpretation of the Penobscot 3D seismic volume using constrained sparse spike inversion, sable sub-Basin, offshore Nova Scotia. Mar. Petrol. Geol. 68, 73–93. https://doi.org/10.1016/j.marpetgeo.2015.08.009.

Celecia, A., Figueiredo, K., Rodriguez, C., Vellasco, M., Maldonado, E., Silva, M.A., Rodrigues, A., Nascimento, R., Ourofino, C., 2021. Unsupervised machine learning applied to seismic interpretation: towards an unsupervised automated interpretation tool. Sensors 21 (19), 6347. https://doi.org/10.3390/s21196347.

Chenin, J., 2020. Examining Seismic Amplitude Responses of Gaseous Media Using Unsupervised Machine Learning. University of Oklahoma.

Chopra, S., Marfurt, K., 2006. Seismic Attributes–a promising aid for geologic prediction: CSEG recorder, 31 (5), 110–120.

Chopra, S., Marfurt, K.J., 2005. Seismic attributes—A historical perspective. Geophysics 70 (5), 3SO–28SO. https://doi.org/10.1190/1.2098670.

Coléou, T., Poupon, M., Azbel, K., 2003. Unsupervised seismic facies classification: a review and comparison of techniques and implementation. Lead. Edge 22 (10), 942–953. https://doi.org/10.1190/1.1623635.

Cummings, D.I., 2004. Sedimentology and Stratigraphy of an Ancient Progradational Terrigenous Clastic Shelf Margin, Missisauga Formation (Upper Jurassic-Lower Cretaceous), Offshore Nova Scotia. University of Ottawa, Canada (Canada).

Cummings, D.I., Hart, B.S., Arnott, R.W.C., 2006. Sedimentology and stratigraphy of a thick, areally extensive fluvial–marine transition, Missisauga Formation, offshore Nova Scotia, and its correlation with shelf margin and slope strata. Bull. Can. Petrol. Geol. 54 (2), 152–174. https://doi.org/10.2113/gscpgbull.54.2.152.

Decalf, C.C., Heyn, T., 2023. Salt geometry in the Central Basin of the Nova Scotia passive margin, offshore Canada based on new seismic data. Mar. Petrol. Geol. 149, 106065. https://doi.org/10.1016/j.marpetgeo.2022.106065.
Deptuck, M.E., Altheim, B., 2018. Rift Basins of the Central LaHave Platform, Offshore Nova Scotia: Canada–Nova Scotia Offshore Petroleum Board Geoscience Open File Report.
Deptuck, M.E., Kendell, K., Brown, D.E., Smith, B.M., 2014. Seismic Stratigraphic Framework and Structural Evolution of the Eastern Scotian Slope: Geological Context for the NS14-1 Call for Bids Area, Offshore Nova Scotia: Nova Scotia, Canada, Canada–Nova Scotia Offshore Petroleum Board. Geoscience Open File Report.
dos Santos, D.T., Roisenberg, M., dos Santos Nascimento, M., 2021. Deep recurrent neural networks approach to sedimentary facies classification using well logs. IEEE Geosci. Remote Sens. Lett. 19, 1–5. https://doi.org/10.1109/LGRS.2021.3053383.
Eleslambouly, A., Abdelmaksoud, A., Ali, M., 2026a. Field characterization and 3D static modeling of the gas-bearing reservoirs, scarborough field, Northern Carnarvon Basin, Australia. Petroleum Research. https://doi.org/10.1016/j.ptlrs.2026.05.001.
Eleslambouly, A., Aldhanhani, O., Fathy, A., Zeynalli, M., Alsuwaidi, M., 2024a. Geothermal plays feasibility and potential in a transform Basin: a case Study from Southern Vienna Basin. In: Proceedings Abu Dhabi International Petroleum Exhibition and Conference. SPE, D031S100R003. https://doi.org/10.2118/222809-MS.
Eleslambouly, A., Aldhanhani, O., Rouxel, S., Zeynalli, M., 2024b. Basin analysis implications for petroleum system modeling: a case study on the Penobscot Field, Nova Scotia, Canada. In: Proceedings Fourth International Meeting for Applied Geoscience & Energy. Society of Exploration Geophysicists and American Association of Petroleum, pp. 1496–1500. https://doi.org/10.1190/image2024-4098485.1.
Eleslambouly, A., Khalifa, T., Aldhanhani, O., Zeynalli, M., Abdelmaksoud, A., 2025. Integrated Field Characterization and Static Hydrocarbon Reserve Estimations of the Penobscot Field. Energy Geoscience, Nova Scotia, Canada, 100448. https://doi.org/10.1016/j.engeos.2025.100448.
Eleslambouly, A., Zeynalli, M., Moncada, A., Fathy, A., Rouxel, S., 2024c. Advancing carbon storage in offshore Louisiana: evaluation and modeling potential of two major depleted reservoirs in Vermilion_014 Field. In: Proceedings Carbon Capture, Utilization, and Storage Conference and Exhibition, pp. 198–217. https://doi.org/10.15530/ccus-2024-4014060. Houston, Texas, USA, Mar 11-13.
Eleslambouly, A., Zhao, G., Bouchaala, F., Ali, M.Y., Matsushima, J., 2026b. Transfer learning with U-Swin transformer for adaptive ground roll attenuation in seismic records from sabkha environments. IEEE Access 14, 30278–30290. https://doi.org/10.1109/ACCESS.2026.3666569.
Eleslambouly, A.K., Zeynalli, M., Al-Shalabi, E.W., Alsuwaidi, M., 2026c. Probabilistic approach for static carbon storage capacity estimation: a case study on the VR014 depleted gas field in offshore Louisiana, USA. Geoenergy Sci. Eng. 260, 214397. https://doi.org/10.1016/j.geoen.2026.214397.
Eliuk, L.S., 1978. The Abenaki Formation, Nova Scotia shelf, Canada—A depositional and diagenetic model for a Mesozoic carbonate platform. Bull. Can. Petrol. Geol. 26 (4), 424–514.
Ellis, P.M., Crevello, P.D., Eliuk, L.S., 1985. Upper Jurassic and Lower Cretaceous deep-water Buildups, Abenaki Formation, Nova Scotia Shelf. SEPM Society for Sedimentary Geology. https://doi.org/10.2110/cor.85.06.0212.
Ercoli, M., Carboni, F., Akimbekova, A., Carbonell, R.B., Barchi, M.R., 2023. Evidencing subtle faults in deep seismic reflection profiles: data preconditioning and seismic attribute analysis of the legacy CROP-04 profile. Front. Earth Sci. 11, 1119554. https://doi.org/10.3389/feart.2023.1119554.
Faleide, T.S., Braathen, A., Lecomte, I., Mulrooney, M.J., Midtkandal, I., Bugge, A.J., Planke, S., 2021. Impacts of seismic resolution on fault interpretation: insights from seismic modelling. Tectonophysics 816, 229008. https://doi.org/10.1016/j.tecto.2021.229008.
Fehmers, G.C., Höcker, C.F., 2003. Fast structural interpretation with structure-oriented filtering. Geophysics 68 (4), 1286–1293. https://doi.org/10.1190/1.1598121.
Gao, D., 2011. Latest developments in seismic texture analysis for subsurface structure, facies, and reservoir characterization: a review. Geophysics 76 (2), W1–W13. https://doi.org/10.1190/1.3553479.
Gao, K., Huang, L., Zheng, Y., Lin, R., Hu, H., Cladohous, T., 2022. Automatic fault detection on seismic images using a multiscale attention convolutional neural network. Geophysics 87 (1), N13–N29. https://doi.org/10.1190/geo2020-0945.1.
Gao, S., Ver Steeg, G., Galstyan, A., 2015. Efficient estimation of mutual information for strongly dependent variables. In: Proceedings Artificial Intelligence and Statistics. PMLR, pp. 277–286.
Gilbert, R.J., Liu, Y., Abriel, W., Preece, R., 2010. Reservoir modeling: integrating various data at appropriate scales. Lead. Edge 23, 784–788. https://doi.org/10.1190/1.1786903.
Given, M., 1977. Mesozoic and early Cenozoic geology of offshore Nova Scotia. Bull. Can. Petrol. Geol. 25 (1), 63–91. https://doi.org/10.35767/gscpgbull.25.1.063.
Gorain, S., Shalivahan, 2018. Application of attribute-based inversion and spectral decomposition with red–green–blue colour blending for visualization of geological features: a case study from the Kalol Field, Cambay Basin, India. Pet. Geosci. 24 (1), 102–111. https://doi.org/10.1144/petgeo2015-090.
Hart, B.S., 1999. Definition of subsurface stratigraphy, structure and rock properties from 3-D seismic data. Earth Sci. Rev. 47 (3–4), 189–218. https://doi.org/10.1016/S0012-8252(99)00029-X.
Hjelm, R.D., Fedorov, A., Lavoie-Marchildon, S., Grewal, K., Bachman, P., Trischler, A., Bengio, Y., 2018. Learning deep representations by mutual information estimation and maximization. arXiv preprint arXiv:1808.06670.
Hudec, M.R., Jackson, M.P., 2006. Advance of allochthonous salt sheets in passive margins and orogens. AAPG Bull. 90 (10), 1535–1564. https://doi.org/10.1306/05080605143.
Hussain, M., Liu, S., Ashraf, U., Ali, M., Hussain, W., Ali, N., Anees, A., 2022. Application of machine learning for lithofacies prediction and cluster analysis approach to identify rock type. Energies 15 (12), 4501. https://doi.org/10.3390/en15124501.
Ikevuje, A.H., Kwakye, J.M., Ekechukwu, D.E., Benjamin, O., 2024. Optimizing the energy mix: strategies for reducing energy dependence: open Access Research. Journal of Multidisciplinary Studies 8 (1), 94–104. https://doi.org/10.53022/oarjms.2024.8.1.0051.
Jamil, A., Hameed, A.A., Orman, Z., 2023. A faster dynamic convergency approach for self-organizing maps. Complex Intell. Syst. 9 (1), 677–696. https://doi.org/10.1007/s40747-022-00826-2.
Jo, I., Lee, S., Oh, S., 2019. Improved measures of redundancy and relevance for mRMR feature selection. Computers 8 (2), 42. https://doi.org/10.3390/computers8020042.
Kendell, K., Deptuck, M., 2012. Lower Cretaceous shelf-edge trajectories, shelf-indenting canyons and the potential transfer of coarser clastics into deeper water. Sable Subbasin, offshore Nova Scotia: Geoscience Open File Poster 2012-002PF, Canada-Nova Scotia Offshore Petroleum Board, 2 panels.
Khalid, P., Ahmed, N., Khan, K.A., Naeem, M., 2015. AVO-derived attributes to differentiate reservoir facies from non-reservoirs facies and fluid discrimination in Penobscot area. Nova Scotia: Geosci. J. 19, 471–480. https://doi.org/10.1007/s12303-014-0048-0.
Khosro Anjom, F., Vaccarino, F., Socco, L.V., 2024. Machine learning for seismic exploration: where are we and how far are we from the holy grail? Geophysics 89 (1), WA157–WA178. https://doi.org/10.1190/geo2023-0129.1.
Kim, Y., Hardisty, R., Marfurt, K.J., 2019. Attribute selection in seismic facies classification: application to a Gulf of Mexico 3D seismic survey and the Barnett Shale. Interpretation 7 (3), SE281–SE297. https://doi.org/10.1190/INT-2018-0246.1.
Kohonen, T., 1982. Self-organized formation of topologically correct feature maps. Biol. Cybern. 43 (1), 59–69. https://doi.org/10.1007/BF00337288.
Kohonen, T., 2001. The Basic SOM: Self-Organizing Maps, pp. 105–176. https://doi.org/10.1007/978-3-642-56927-2_3.
Laudon, C., Qi, J., Rondon, A., Rouis, L., Kabazi, H., 2021. An enhanced fault detection workflow combining machine learning and seismic attributes yields an improved fault model for Caspian Sea asset. First Break 39 (10), 53–60. https://doi.org/10.3997/1365-2397.fb2021075.
Lin, L., Zhong, Z., Li, C., Gorman, A., Wei, H., Kuang, Y., Wen, S., Cai, Z., Hao, F., 2024. Machine learning for subsurface geological feature identification from seismic data: methods, datasets, challenges, and opportunities. Earth Sci. Rev., 104887 https://doi.org/10.1016/j.earscirev.2024.104887.
Lister, D.L., 2004. Modelling Fault Geometry and Displacement for Very Large Networks.
Mandal, A., Srivastava, E., 2018. Enhanced structural interpretation from 3D seismic data using hybrid attributes: new insights into fault visualization and displacement in Cretaceous formations of the Scotian Basin, offshore Nova Scotia. Mar. Petrol. Geol. 89, 464–478. https://doi.org/10.1016/j.marpetgeo.2017.10.013.
Meyer, S., Reading, A., Bassom, A., 2022. The use of weighted self-organizing maps to interrogate large seismic data sets. Geophys. J. Int. 231 (3), 2156–2172. https://doi.org/10.1093/gji/ggac322.
Michie, E.A., Mulrooney, M.J., Braathen, A., 2021. Fault interpretation uncertainties using seismic data, and the effects on fault seal analysis: a case study from the Horda Platform, with implications for $CO_2$ storage. Solid Earth 2021, 1–46. https://doi.org/10.5194/se-12-1259-2021.
Miyoshi, T., Kawai, H., Masuyama, H., 2002. Efficient SOM learning by data order adjustment. In: Proceedings of the 2002 International Joint Conference on Neural Networks, vol. 1. IEEE, pp. 784–787. IJCNN'02 (Cat. No. 02CH37290).
Mora, J.P., Bedle, H., Marfurt, K.J., 2022a. Fault enhancement comparison among coherence enhancement, probabilistic neural networks, and convolutional neural networks in the Taranaki Basin area, New Zealand. Interpretation 10 (3), SE1–SE19. https://doi.org/10.1190/int-2021-0151.1.
Mora, J.P., Bedle, H., Marfurt, K.J., 2022b. Fault enhancement using probabilistic neural networks and Laplacian of a Gaussian filter: a case study in the Great South Basin, New Zealand. Interpretation 10 (2), SC1–SC15. https://doi.org/10.1190/INT-2021-0127.1.
Moreno, W.E.G., Galeano, I.D.O., 2019a. Identification of high velocity anomalies, imperceptible to seismic resolution, by integration of seismic attributes, in penobscot field. Canada: Rudarsko-Geolosko-Naftni Zb. 34 (1), 13–26. https://doi.org/10.17794/rgn.2019.1.2.
Moreno, W.E.G., Galeano, I.D.O., 2019b. Solution of High Velocity Anomalies Imperceptible to Seismic Resolution, by Means of Synthetic Models, Penobscot Field. The Mining-Geology-Petroleum Engineering Bulletin, Canada. https://doi.org/10.17794/rgn.2019.1.7.
Mukhopadhyay, P.K.M., Brown, D.E., Kidston, A.G., Bowman, T.D., Faber, J., Harvey, P.J., 2003. Petroleum systems of deepwater Scotian Basin, Eastern Canada: challenges for finding oil versus gas provinces. In: Proceedings Offshore Technology Conference. OTC. https://doi.org/10.4043/15304-MS. OTC-15304-MS.

Narayan, S., Sahoo, S.D., Pal, S., Pham, L., Kumar, P., 2023. Integrated geophysical and petrophysical characterization of Upper Jurassic carbonate reservoirs from Penobscot field, Nova Scotia: a case study. Marine Geophysical Research 44 (4), 23. https://doi.org/10.1007/s11001-023-09533-0.

Omeru, T., Bankole, S.I., Jolly, B.A., Seyi, O.S., Omojola, J.B., 2019. Assessment of the effect of mass-transport deposits on fault propagation in Penobscot area, offshore Nova Scotia. Geological Society, London, Special Publications 477 (1), 121–131. https://doi.org/10.1144/sp477.23.

Oumarou, S., Mabrouk, D., Tabod, T.C., Marcel, J., Ngos III, S., Essi, J.M.A., Kamguia, J., 2021. Seismic attributes in reservoir characterization: an overview. Arabian J. Geosci. 14, 1–15. https://doi.org/10.1007/s12517-021-06626-1.

Owusu, B.A., Boateng, C.D., Asare, V.-D.S., Danuor, S.K., Adenutsi, C.D., Quaye, J.A., 2024. Seismic facies analysis using machine learning techniques: a review and case study. Earth Sci. Inf. 17 (5), 3899–3924. https://doi.org/10.1007/s12145-024-01395-3.

Pe-Piper, G., MacKay, R., 2006. Provenance of Lower Cretaceous sandstones onshore and offshore Nova Scotia from electron microprobe geochronology and chemical variation of detrital monazite. Bull. Can. Petrol. Geol. 54 (4), 366–379. https://doi.org/10.2113/gscpgbull.54.4.366.

Peace, A.L., Phethean, J.J., Jess, S., Schiffer, C., 2024. Halokinetically overprinted tectonic inversion of the penobscot 3D volume offshore Nova Scotia, Canada. Pure Appl. Geophys. 181 (5), 1541–1570. https://doi.org/10.1007/s00024-024-03462-8.

Provenzano, G., Vardy, M.E., Henstock, T.J., 2017. Pre-stack full waveform inversion of ultra-high-frequency marine seismic reflection data. Geophysical journal international 209 (3), 1593–1611. https://doi.org/10.1093/gji/ggx114.

Qayyum, F., Catuneanu, O., Bouanga, C.E., 2015. Sequence stratigraphy of a mixed siliciclastic-carbonate setting, Scotian Shelf, Canada. Interpretation 3 (2), SN21–SN37. https://doi.org/10.1190/int-2014-0129.1.

Qi, J., Machado, G., Marfurt, K., 2017. A workflow to skeletonize faults and stratigraphic features. Geophysics 82 (4), O57–O70. https://doi.org/10.1190/geo2016-0641.1.

Ramsey, M., 2019. Schlumberger Oilfield Glossary: SLB, vol. 9, p. 2024. URL: glossary.slb.com/.

Rashid, M., Luo, M., Ashraf, U., Hussain, W., Ali, N., Rahman, N., Hussain, S., Aleksandrovich Martyushev, D., Vo Thanh, H., Anees, A., 2022. Reservoir quality prediction of gas-bearing carbonate sediments in the Qadirpur field: insights from advanced machine learning approaches of SOM and cluster analysis. Minerals 13 (1), 29. https://doi.org/10.3390/min13010029.

Roden, R., Smith, T., Sacrey, D., 2015. Geologic pattern recognition from seismic attributes: principal component analysis and self-organizing maps. Interpretation 3 (4), SAE59–SAE83. https://doi.org/10.1190/int-2015-0037.1.

Rotimi, O.J., Ako, B.D., Wang, Z., 2014. Reservoir characterization and modeling of lateral heterogeneity using multivariate analysis. Energy Explor. Exploit. 32 (3), 527–552. https://doi.org/10.1260/0144-5987.32.3.527.

Sayers, J., 2013. Enhancement of the Geological Features of the Scotian Basin by the Application of Spectral Inversion, Offshore Nova Scotia.

Schenk, P.E., 1997. Sequence stratigraphy and proveance on Gondwana's margin: the Meguma Zone (Cambrian to Devonian) of Nova Scotia, Canada. Geol. Soc. Am. Bull. 109 (4), 395–409. https://doi.org/10.1130/0016-7606(1997)109<0395:SSAPOG>2.3.CO;2.

Shi, Y., Liao, J., Gan, L., Tang, R., 2024. Lithofacies prediction from well log data based on deep learning: a case study from Southern Sichuan, China. Appl. Sci. 14 (18), 8195. https://doi.org/10.3390/app14188195.

Shimeld, J., 2004. A comparison of salt tectonic subprovinces beneath the Scotian Slope and Laurentian Fan. In: Salt Sediment Interactions and Hydrocarbon Prospectivity Concepts, Applications and Case Studies for the 21st Century, vol. 24. https://doi.org/10.5724/gcs.04.24.0502.

Shiney, S.A., Seetharaman, R., Sharmila, V., Prathiba, S., 2025. Deep learning based gasket fault detection: a CNN approach. Sci. Rep. 15 (1), 4776. https://doi.org/10.1038/s41598-025-85223-8.

Smith, R., 2015. A mutual information approach to calculating nonlinearity. Stat 4 (1), 291–303. https://doi.org/10.1002/sta4.96.

Song, Y., Tang, Y., He, W., Gong, D., Yan, Q., Chen, G., Shan, X., Liu, C., Liu, G., Qin, Z., 2024. New fields, new types and exploration potentials of oil-gas exploration in Junggar Basin. Acta Pet. Sin. 45 (1), 52. https://doi.org/10.7623/syxb202401004.

Straub, K.M., Paola, C., Mohrig, D., Wolinsky, M.A., George, T., 2009. Compensational stacking of channelized sedimentary deposits. J. Sediment. Res. 79 (9), 673–688. https://doi.org/10.2110/jsr.2009.070.

Su, M.-C., Chang, H.-T., 2001. A new model of self-organizing neural networks and its application in data projection. IEEE Trans. Neural Network. 12 (1), 153–158. https://doi.org/10.1109/72.896805.

Subrahmanyam, D., Rao, P., 2008. Seismic attributes-a review. In: Proceedings 7th International Conference and Exposition on Petroleum Geophysics. Hyderabad, India.

Swisi, A.A., 2009. Post-And Pre-stack Attribute Analysis and Inversion of Blackfoot 3Dseismic Dataset. University of Saskatchewan.

van der Meer, F., 1996. Spectral mixture modelling and spectral stratigraphy in carbonate lithofacies mapping. ISPRS J. Photogrammetry Remote Sens. 51 (3), 150–162. https://doi.org/10.1016/0924-2716(95)00009-7.

van Staal, C.R., Barr, S.M., Percival, J., Cook, F., Clowes, R., 2012. Lithospheric Architecture and Tectonic Evolution of the Canadian Appalachians and Associated Atlantic Margin, Tectonic Styles in Canada: the LITHOPROBE Perspective, vol. 49. Geological Association of Canada Special Paper, pp. 41–95.

Wach, G.D., Brown, D.E., 2021. Petroleum Exploration on the Scotian Margin: Geoconvention, vol. 7.

Wade, J., MacLean, B., 1990. The geology of the southeastern margin of Canada. Geology of the Continental Margin of Eastern Canada.

Waldeland, A.U., Jensen, A.C., Gelius, L.-J., Solberg, A.H.S., 2018. Convolutional neural networks for automated seismic interpretation. Lead. Edge 37 (7), 529–537. https://doi.org/10.1190/tle37070529.1.

Wang, G., Carr, T.R., 2012. Methodology of organic-rich shale lithofacies identification and prediction: a case study from Marcellus Shale in the Appalachian basin. Comput. Geosci. 49, 151–163. https://doi.org/10.1016/j.cageo.2012.07.011.

Wu, G., Kong, F., Tian, N., Ma, T., Tao, C., 2023. Structural characteristics and deep-water hydrocarbon accumulation model of the Scotian Basin, Eastern Canada. Energy Geoscience 4 (3), 100152. https://doi.org/10.1016/j.engeos.2022.100152.

Wu, X.-H., Bi, L., Kalla, S., 2012. Effective parametrization for reliable reservoir performance predictions: International Journal for Uncertainty Quantification, 2 (3). https://doi.org/10.1615/Int.J.UncertaintyQuantification.2012003765.

Xu, Z., Liu, J., Luo, X., Yang, Z., Zhang, Y., Yuan, P., Tang, Y., Zhang, T., 2019. Software defect prediction based on kernel PCA and weighted extreme learning machine. Inf. Software Technol. 106, 182–200. https://doi.org/10.1016/j.infsof.2018.10.004.

Yagci, F.G., 2016. Reprocessing and Structural Interpretation of Multichannel Seismic Reflection Data from Penobscot. Nova Scotia: Missouri University of Science and Technology.

Zhang, Y., Zheng, X.-D., Li, J.-S., Lu, J.-T., Cao, C.-Y., Sui, J.-K., 2015. Unsupervised seismic facies analysis technology based on SOM and PSO. Chin. J. Geophys. 58 (9), 3412–3423. https://doi.org/10.6038/cjg20150933.

Zhao, T., Jayaram, V., Roy, A., Marfurt, K.J., 2015. A comparison of classification techniques for seismic facies recognition. Interpretation 3 (4), SAE29–SAE58. https://doi.org/10.1190/INT-2015-0044.1.

Zhao, T., Mukhopadhyay, P., 2018. A fault detection workflow using deep learning and image processing. In: Proceedings SEG International Exposition and Annual Meeting. SEG. https://doi.org/10.1190/segam2018-2997005.1. SEG-2018-2997005.

Zhu, D., Li, L., Guo, R., Tao, C., Zhan, S., 2022. 3D fault detection: using human reasoning to improve performance of convolutional neural networks. Geophysics 87 (4), IM143–IM156. https://doi.org/10.1190/geo2020-0905.1.